

**Report for AOARD Grant FA2386-11-1-4105**

**Uncovering the Physical Basis Connecting Environment and  
Tribological Performance of Ultrananocrystalline Diamond**

**Submitted to:  
THE ASIAN OFFICE  
OF AEROSPACE RESEARCH & DEVELOPMENT**

**Submitted by:**

**Department of Mechanical Engineering,  
National Chung Cheng University**

**Yeau-Ren Jeng, Professor  
Department of Mechanical Engineering,  
National Chung Cheng University,  
Ming-Hsiung, Chia-Yi 621,  
TAIWAN**

**E-mail: [imeyrj@ccu.edu.tw](mailto:imeyrj@ccu.edu.tw)**

**Tel: 886-5-2428189**

**Fax: 886-5-2720589**

Report Documentation Page				Form Approved OMB No. 0704-0188	
Public reporting burden for the collection of information is estimated to average 1 hour per response, including the time for reviewing instructions, searching existing data sources, gathering and maintaining the data needed, and completing and reviewing the collection of information. Send comments regarding this burden estimate or any other aspect of this collection of information, including suggestions for reducing this burden, to Washington Headquarters Services, Directorate for Information Operations and Reports, 1215 Jefferson Davis Highway, Suite 1204, Arlington VA 22202-4302. Respondents should be aware that notwithstanding any other provision of law, no person shall be subject to a penalty for failing to comply with a collection of information if it does not display a currently valid OMB control number.					
1. REPORT DATE <b>17 APR 2014</b>		2. REPORT TYPE <b>Final</b>		3. DATES COVERED <b>18-08-2011 to 17-08-2013</b>	
4. TITLE AND SUBTITLE <b>Uncovering the Physical Basis Connecting Environment and Tribological Performance of Ultrananocrystalline Diamond</b>				5a. CONTRACT NUMBER <b>FA23861114105</b>	
				5b. GRANT NUMBER	
				5c. PROGRAM ELEMENT NUMBER	
6. AUTHOR(S) <b>Yeau-Ren Jeng</b>				5d. PROJECT NUMBER	
				5e. TASK NUMBER	
				5f. WORK UNIT NUMBER	
7. PERFORMING ORGANIZATION NAME(S) AND ADDRESS(ES) <b>National Chung Cheng University,168, University Road, Minh-Siung,Chia-Yi 62102,Taiwan,NA,NA</b>				8. PERFORMING ORGANIZATION REPORT NUMBER <b>N/A</b>	
9. SPONSORING/MONITORING AGENCY NAME(S) AND ADDRESS(ES) <b>AOARD, UNIT 45002, APO, AP, 96338-5002</b>				10. SPONSOR/MONITOR'S ACRONYM(S) <b>AOARD</b>	
				11. SPONSOR/MONITOR'S REPORT NUMBER(S) <b>AOARD-114105</b>	
12. DISTRIBUTION/AVAILABILITY STATEMENT <b>Approved for public release; distribution unlimited</b>					
13. SUPPLEMENTARY NOTES					
14. ABSTRACT <b>The researchers have studied the nano-scale mechanical and tribological properties of ultrananocrystalline diamond (UNCD), which is a thin-film material known to have extremely high strength and excellent tribological properties, namely low friction, adhesion, and wear, at macroscopic scales. They have successfully grown UNCD films in house and characterized their composition and structure. They have measured the surface chemical properties of these samples as well as commercial UNCD samples from their collaborator, Advanced Diamond Technologies Inc. Measurements demonstrate the expected carbon-rich composition but with measureable amounts of surface-bound contaminants. They also performed TEM observations to investigate the grain structure of commercial UNCD films, verifying a nanoscale grain size. They worked with collaborators from UPenn on in-situ TEM nanoindentation methodology and obtained preliminary results characterizing the adhesion and wear behavior of computational nano-scale UNCD asperities, verifying extremely low wear particularly in comparison to Si.</b>					
15. SUBJECT TERMS <b>Modelling &amp; Simulation, multiscale modeling , Nanoscale mechanics, Ultrananocrystalline Daimond</b>					
16. SECURITY CLASSIFICATION OF:			17. LIMITATION OF ABSTRACT <b>Same as Report (SAR)</b>	18. NUMBER OF PAGES <b>46</b>	19a. NAME OF RESPONSIBLE PERSON
a. REPORT <b>unclassified</b>	b. ABSTRACT <b>unclassified</b>	c. THIS PAGE <b>unclassified</b>			



## **Abstract**

We have studied the growth and the nanoscale mechanical and tribological properties of high-strength carbon-based thin films, including nanocrystalline diamond (NCD) and ultrananocrystalline diamond (UNCD). We are able to grow high quality NCD films on substrates and on nanoscale atomic force microscope tips. Using in situ transmission electron microscopy-based nanoscale wear measurements, we also show that commercial UNCD films are highly wear resistant compared with silicon and diamondlike carbon (DLC). We find that boron-doping of UNCD alters the nanostructure of the film but has minimal effect on the mechanical properties (namely, modulus and hardness). We show that surface roughness has a strong effect on the adhesion of UNCD and DLC surfaces. Finally, we show that, during sliding, a key wear mechanism in UNCD and tetrahedral amorphous carbon (ta-C) films involves rehybridization of carbon from  $sp^3$  to  $sp^2$  hybridization, and the rate occurs more quickly for ta-C than UNCD due to the pre-stressed nature of the bonds. In total, these results help advance the scientific understanding of the mechanical and tribological properties of functional carbon-based coatings which have potential for multiple Air Force applications. Finally, the U. Pennsylvania research team visited CCU in June 2013. We worked together on our in-situ TEM nanoindentation methodology and obtained significantly results characterizing the tribological behaviors of nano-scale UNCD asperities, verifying preliminary wear might be governed by interatomic adhesion.

## 1. Introduction

Nanotechnology is leading to the development of materials and devices whose structure and function are controlled down to the atomic scale. Many such applications have components that experience mechanical contact and sliding. However, the lack of understanding of tribology (adhesion, friction, and wear) at a fundamental level is preventing such systems from being viable. Tribology is critical due to the high surface-to-volume ratio intrinsic to small devices. Indeed, critical problems in the reliability of micro- and nano-electromechanical systems (MEMS/NEMS) devices due to friction- and wear-related failures is well documented [1, 2].

Ultrastrong coatings hold promise for addressing these problems. In particular, nanocrystalline and ultrananocrystalline diamond (NCD and UNCD) solid lubricant thin films exhibit remarkably low friction and wear at both macroscopic and nanoscopic scales [3-7]. The tribological properties of NCD films: roughness, thickness, elastic modulus, and surface chemistry, are all affected by the conditions under which the film is grown in the Hot Filament Chemical Vapor Deposition System (HFCVD). Each of these properties contributes to the wear resistance and friction coefficient of the NCD film. To this end we have studied the effect of temperature, methane dilution, and growth time on the roughness and thickness of deposited NCD films.

UNCD alone has low electrical conductivity, which makes it unattractive for applications in nano-electronic systems. Boron-doping of UNCD is a novel way to prepare these films for use in MEMS/NEMS devices. For this

project we studied the effect of Boron doping on the grain size, hardness, roughness, and adhesion of UNCD coated Silicon probes. Data on the effect of film deposition temperature on the grain size and Carbon bonding spectrum was taken using a Synchrotron-based near-edge X-ray absorption fine structure (NEXAFS). The hardness of B-doped UNCD atomic force microscopy (AFM) probes was measured with a Hysitron Triboindenter while their rate of wear due to mechanical contact sliding was studied in-situ using a JEOL 2100 Transmission Electron Microscope (TEM) for imaging and a Hysitron PI-95 Picoindenter for controlling the mechanical contact conditions of the test.

## **2. Methodology**

### **Experiment**

#### **I. Hot Filament Chemical Vapor Deposition System (HFCVD)**

For UNCD film growth, we use a hot filament chemical vapor deposition system (HFCVD) at U. Penn (Fig. 1).

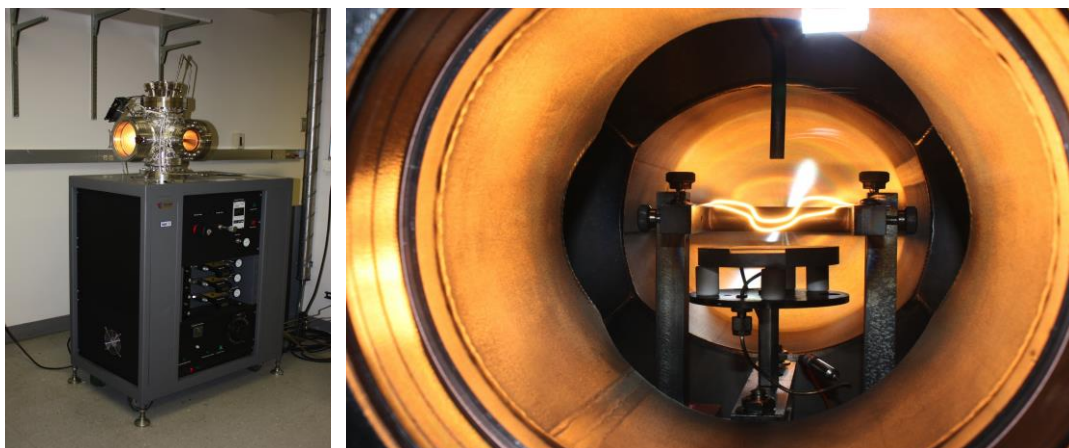


***Fig 1. Left: the HFCVD system. Right: inside view of diamond film growth showing the gas entry tube above the heated filaments, with the sample below.***

This commercial system from BlueWave Semiconductor has been customized for nanocrystalline diamond growth [8]. The UHV-compatible chamber operates a base pressure of  $\sim 2 \times 10^{-3}$  Torr. Decomposition of precursor gas species is accomplished with two 0.020-in.-diameter tungsten filaments. The substrate to be coated, usually a silicon wafer, sits below the filament on a 25 mm diameter heating stage which can heat samples up to 750°C. The substrate will also be heated by the filaments themselves. Whenever new tungsten filaments were installed, a methane pretreatment was performed. With 9 sccm methane at 10-20 Torr, the filaments were heated to approximately 1500°C for 10 minutes, then at 1800-1900°C for 5 minutes and finally for a brief moment at 2100°C to form a thin tungsten carbide layer, which prevents tungsten evaporation during subsequent film growth. As expected, there was no sign of W contamination on any samples as verified by X – ray photoemission spectroscopy. Filament temperatures are measured with an infrared pyrometer (550-3200°C). The substrates were coated with diamond nanoparticles (ITC Inc.) which serve as nucleation sites for diamond growth. The sample is inserted into the chamber. Precursor gases of methane at 3.7 sccm and hydrogen at 90 sccm are introduced into the chamber at an operating pressure of approximately 30 Torr with the sample temperature set to  $\sim 700$  °C.

## **II. X-Ray Photoelectron Spectroscopy (XPS)**

XPS is used to characterize the composition and chemical bonding state

of the top 2-4 nm of the surface of the sample. The XPS analyses were carried out with a customized X-ray photoelectron spectrometer (a VG Scienta R3000 customized for elevated pressure operation), which is extensively been described in reference [9]. Briefly, the spectrometer is equipped with a monochromatic Al K $\alpha$  source (VG Scienta MX 650). The electrons emitted from the specimen are collected with an electrostatic lens, whose axis is normal to the sample surface. After passing the hemispherical analyzer, the photoelectrons are detected by a two-dimensional MCP/CCD detector. In the present work, the X-ray source was run at 30 mA and 12 kV in high vacuum ( $<10^{-8}$  Torr) conditions, and the analyzer was operated in constant-analyzer-energy mode. A differential pumping system operating on the analyzer and electron optics column allows XPS operation in gaseous environments, up to 0.4 Torr. This capability will be used in the future to investigate the environmental dependence of the surface chemistry as a function of exposure to water vapor.

### **III. Transmission electron microscopy (TEM) and In-Situ Nanoindentation**

Two TEM systems have been used for the research at U. Penn. The first is a JEOL 2010F Field-Emission TEM/STEM. This is a state-of-the-art field emission transmission electron microscope with capabilities ranging from nanobeam and convergent beam diffraction to high resolution phase contrast, analytical and energy filtered imaging. The 2010F has been optimized for analytical microscopy with a large solid angle for high X-ray throughput,



scanning, scanning-transmission, and backscattered electron detectors and a Gatan image filter for energy filtered imaging and electron energy loss spectroscopy. This combination of analytical capabilities makes the 2010F ideal for the characterization of a wide array of samples, but it is also a very capable high-resolution instrument with a point-to-point resolution of 0.23 nm. The second TEM at U. Penn is a JEOL 2010 TEM, available for both conventional and high resolution TEM imaging. It is equipped with single tilt, double-tilt, heating and cooling sample holders for a wide range of imaging experiments. The analytical objective lens pole piece on this microscope allows for sample tilting up to 45 degrees, while maintaining a point-to-point resolution of 0.25 nm. In addition to the conventional plate camera, this instrument is equipped with a Gatan Peltier cooled CCD imaging system for high quality digital imaging.

Nanoscale wear tests were conducted inside either the JEOL 2010F transmission electron microscope (TEM) at U. Penn, or inside a JEOL TEM at CCU, using an in situ nanoindentation apparatus (PI-95, Hysitron, Minneapolis, MN). A nominally flat (100)-oriented diamond punch was brought into contact with a series of sharp ( $R < 100$  nm) asperities (single crystal silicon, initially terminated with silicon oxide, or UNCD). The Si tips were model PPP-CONTR, (Nanosensors, Neuchatel, Switzerland), and the UNCD tips were custom probes provided by ADT, Inc. The tips were formed by coating commercial Si cantilevers with a UNCD film. Since the asperities are comprised of the ends of AFM tips which are integrated with microcantilevers, the cantilever deflection allows us to sensitively measure the applied force. Once in contact with a given tip, the

diamond was then slid laterally, with reciprocating strokes typically of 100 nm, with only the adhesive force acting (no additional applied load). The contact was separated at varying intervals throughout the wear test to measure the instantaneous adhesive force, determined by observing the tensile deflection of the calibrated cantilever upon separation. Tips of varying shape were tested, with total sliding distances ranging from 200 nm to a few  $\mu\text{m}$  for each test. All sliding was recorded with real-time video, and high resolution (lattice-resolved, when possible) TEM images of the asperities were taken upon each separation. In post-processing, the instantaneous asperity profile was traced using the out-of-contact images. Then the profiles were integrated to three-dimensional shapes (assuming axisymmetry of each differential slice) to quantify the volume removed - and thus the number of atoms removed.

## **Approach**

### **I. Nano-mechanics Computational Algorithm**

In this approach, atoms are regarded as nodes, and their potentials are considered to be elements. It is assumed that atom,  $i$ , is located at position  $(x_i, y_i, z_i)$  with displacements  $u_i$ ,  $v_i$  and  $w_i$  in the  $x$ -,  $y$ - and  $z$ -directions, respectively. By defining the nodal displacement vector for the  $i$  atom as  $\{u\}_i$  and the corresponding external nodal force vector as  $\{F\}_i = (f_i, g_i, h_i)^T$ , the total potential energy for atom,  $i$ , can be expressed as:

$$E_i = \frac{1}{2} \sum_{j \neq i} \phi(r_{ij}) + F \left( \sum_{j \neq i} f(r_{ij}) \right) - \{u\}_i^T \{F\}_i \quad (1)$$

where the atomic distance  $r_{ij}$  is given by:

$$r_{ij} = \left\{ (x_i + u_i - x_j)^2 + (y_i + v_i - y_j)^2 + (z_i + w_i - z_j)^2 \right\}^{1/2} \quad (2)$$

The differential of the atomic distance with respect to  $\{u\}_i$  be expressed as:

$$dr_{ij} = \frac{1}{r_{ij}} [x_i + u_i - x_j, y_i + v_i - y_j, z_i + w_i - z_j] d\{u\}_i = [B] d\{u\}_i \quad (3)$$

The principle of minimum work enforces the minimization of the total energy of

the whole system ( $E_{total} = \sum_i E_i$ ) with respect to  $\{u\}_i$  such that:

$$\frac{\partial E_{total}}{\partial \{u\}_i} = \sum_{j \neq i} \left[ \frac{\partial F}{\partial \rho_i} \frac{\partial f}{\partial r_{ij}} + \frac{\partial F}{\partial \rho_j} \frac{\partial f}{\partial r_{ij}} + \frac{\partial \phi}{\partial r_{ij}} \right] - \{F\}_i = \{0\} \quad (4)$$

Equation (8) expresses the equilibrium equation at atom 'i', which represents the equilibrium of the forces acting on atoms 'i'.

The unbalance force,  $\{\xi\}_i$ , can then be defined as:

$$\{\xi\}_i = \sum_{j \neq i} \left[ \frac{\partial F}{\partial \rho_i} \frac{\partial f}{\partial r_{ij}} + \frac{\partial F}{\partial \rho_j} \frac{\partial f}{\partial r_{ij}} + \frac{\partial \phi}{\partial r_{ij}} \right] - \{F\}_i \quad (5)$$

In order to solve this nonlinear equilibrium equation in an efficient iterative way,

it is necessary to differentiate  $\{\xi\}_i$  with respect to  $\{u\}_i$ , i.e.

$$d\{\xi\}_i = \left\{ \begin{aligned} & \frac{\partial^2 F}{\partial \rho_i^2} \left( \sum_{j \neq i} \frac{\partial F}{\partial \rho_i} \frac{[B]}{r_{ij}} \right) \left( \sum_{j \neq i} \frac{\partial F}{\partial \rho_j} \frac{[B]^T}{r_{ij}} \right) \\ & + \sum_{j \neq i} \left\{ \left( \frac{\partial F}{\partial \rho_i} + \frac{\partial F}{\partial \rho_j} \right) \left[ \left( \frac{\partial^2 f}{\partial r_{ij}^2} - \frac{1}{r_{ij}} \frac{\partial f}{\partial r_{ij}} \right) [B][B]^T + \frac{1}{r_{ij}} \frac{\partial f}{\partial r_{ij}} [I] \right] \right\} \\ & + \sum_{j \neq i} \left[ \left( \frac{\partial^2 \phi}{\partial r_{ij}^2} - \frac{1}{r_{ij}} \frac{\partial \phi}{\partial r_{ij}} \right) [B][B]^T + \frac{1}{r_{ij}} \frac{\partial \phi}{\partial r_{ij}} [I] \right] \end{aligned} \right\} d\{u\}_i \quad (6)$$

$$= [K_T]_i d\{u\}_i$$

Subsequently, the conventional finite element formulation assembly procedure can be employed to assemble Equation (8) in order to obtain the total system equation, i.e.

$$d\{\xi\} = [K_T]d\{u\} \quad (7)$$

Similarly, Equation (7) can be assembled to obtain the equilibrium equation of the total system, i.e.

$$\sum_i \xi_i = \{f\}_{\text{internal}} - \{F\}_{\text{external}} = \{0\} \quad (8)$$

In terms of the finite element formulation, Equation (11) represents the tangent stiffness equation, while the terms  $\{f\}_{\text{internal}}$  and  $\{F\}_{\text{external}}$  in Equation (12) denote the internal force vector and the external force vector, respectively. The simulation adopts the Newton-Raphson iterative technique to solve Equation (12) via the displacement control scheme or force control scheme. The need to calculate the full matrix of second derivatives in Newton-Raphson method can restrain the size of the simulated system. Therefore, the present research has developed an algorithm such as the utilization of the block-diagonal Newton-Raphson method to release this limitation. One of the challenges of nano-scale simulation is to predict the long-time system level performances. Hence, there is an imminent need to develop a multi-scale technique to bridge the gap between nano-scale and micro-scale. In this follow-up project, the present research has also developed a coarse graining technique for the multi-scale simulation.

For the simulations of nano-scale thin film nanoindentation, the simulated system configurations include a perfect three-dimensional crystalline slab of atoms with a (001) surface, and an indenter has a triangular pyramidal form. In the simulation, it is assumed that the hardness of the indenter's diamond tip far exceeds that of the thin copper film. Hence the indenter deformation may

be neglected during the indentation process. The simulation assumes boundary conditions in which the atoms located at the four sides and base of the simulated film are fully constrained. The interatomic potential of the substrate is modeled using the Sutton-Chen potential, which has the same functional form in an EAM potential as follows:

$$U = \sum_i U_i \quad (9)$$

$$U_i = \frac{1}{2} \sum_{j \neq i} \phi(r_{ij}) + F(\rho_i) = \varepsilon \left( \frac{1}{2} \sum_{j \neq i} \left( \frac{a}{r_{ij}} \right)^n - c \sqrt{\rho_i} \right) \quad (10)$$

where  $\rho_i$  is an electron density-like term for atom  $i$ , which is defined as:

$$\rho_i = \sum_{j \neq i} f(r_{ij}) = \sum_{j \neq i} \left( \frac{a}{r_{ij}} \right)^m \quad (11)$$

where  $r_{ij}$  is the distance between atoms  $i$  and  $j$ . The potential between the carbon and copper atoms is simulated using the Born-Mayer potential, which only produces an impulsive force. This potential has the following form:

$$\phi(r_{ij}) = A \exp [ -2\alpha ( r_{ij} - r_0 ) ] \quad (12)$$

where  $r_{ij}$  is the distance between carbon atom  $i$  and substrate atom  $j$ . This modified-FEM approach is used to perform simulations of nanoindentation. The distribution of the resulting stress and strain is then examined to clarify the atomic plastic behavior induced during the nanoindentation cycle. We also performed experiments using depth-sensing indentation technique. The load-depth curves of the experiments have been compared with those of computer simulation by the present approach. The indentation size effect and void effect are explored and discussed.

In addition, this study also utilizes molecular simulations to investigate the physical characteristics and the mechanical properties of carbon nanotubes (CNTs). The present research employs the Tersoff–Brenner many-body potential [10-12] to describe the inter-atomic forces, elastic properties, molecular bond energies, and bond lengths of the nanotubes. It has been used successfully by several researchers to model straight carbon nanotubes and to generate accurate predictions of the thermal properties of carbon nanotubes. The Tersoff–Brenner many-body potential is taken to have the form:

$$E = \sum_i E_i = \frac{1}{2} \sum_{i \neq j} V_{ij} \quad (13)$$

$$V_{ij} = f_c(r_{ij})[V_R(r_{ij}) + b_{ij}V_A(r_{ij})] \quad (14)$$

Here,  $E$  is the total energy of the system, which is decomposed for convenience into site energy  $E_i$  and a bond  $V_{ij}$ . The indices  $i$  and  $j$  run over the atoms of the system, and  $r_{ij}$  is the distance from atom  $i$  to atom  $j$ . The cutoff function,  $f_c(r_{ij})$ , is simply taken as

$$f_c(r) = \begin{cases} 1, & r < R - D \\ \frac{1}{2} - \frac{1}{2} \sin \left[ \frac{\pi}{2} (r - R) / D \right], & R - D < r < R + D \\ 0, & r > R + D \end{cases} \quad (15)$$

which has continuous value and derivative for all  $r$ , and goes from 1 to 0 in a small range around  $R$ .  $R$  is chosen to include only the first-neighbor shell for most structures of interest. The short range of the potential is numerically advantageous in many applications, and is important for the applicability of

the simple ideas about coordination discussed here.

The potential itself contains a repulsive and an attractive part,  $V_R$  and  $V_A$ , that both have the exponential:

$$V_R(r) = A \exp^{-\lambda_1 r} \quad (16)$$

$$V_A(r) = B \exp^{-\lambda_2 r} \quad (17)$$

In the present work,  $b_{ij}$  is taken to have the following from:

$$b_{ij} = (1 + \beta^n \xi_{ij})^{-1/2n} \quad (18)$$

where

$$\xi_{ij} = \sum_{k \neq i, j} f_c(r_{ik}) g(\theta_{ijk}) \exp \lambda_3^3 (r_{ij} - r_{ik})^3 \quad (19)$$

$$g(\theta_{ijk}) = 1 + \frac{c^2}{d^2} - \frac{c^2}{[d^2 + (h - c \cos \theta_{ijk})^2]} \quad (20)$$

where  $b_{ij}$  measures the relative strength of the attraction between atoms  $i$  and  $j$ , which depends on the parameters  $\beta$  and  $n$ , and the function,  $\xi_{ij}$ , which measures the total effect of all nearby atoms on the interaction. The  $f_c(r_{ij})$  is again used to remove the effect of the more distant atoms from the calculation and the angular positions of the atoms are modeled with the function,  $g(\theta_{ijk})$ , where  $\theta_{ijk}$  is the angle between atoms  $j$  and  $k$ , measured from atom  $i$ , and the parameters  $A$ ,  $B$ ,  $\lambda_1$ ,  $\lambda_2$ ,  $\lambda_3$ ,  $c$ ,  $d$  and  $h$  are determined through fitting to experimental data. The present research systematically establishes a detailed definition of the mechanical properties of carbon nanotubes during the elastic and plastic deformation.

## **II. Clustered atomistic-continuum mechanics (CACM)**

A novel clustered atomistic-continuum mechanics (CACM) based on the atomic mechanics and nonlinear transient finite element theory is proposed herein to simulate the mechanical behavior of the nano/bulk-structure under external mechanical loading or with thermal condition. In order to reduce the computational time efficiently and makes the simulation of the mechanical behavior of nano- and bulk- structure possible, the CACM treats the specific clustered atoms or molecule groups as a clustered super-element in the modeling, e.g. the sugar-phosphate backbone of DNA, super lattice of metal, and silicon. The cluster atom/molecule, namely super-atom/super-molecule should have the similar mechanical behavior with its discrete form. Moreover, the virtual super-element is adopted to describe the interaction energy/force between atoms or clustered-atom groups (e.g., hydrogen bond, covalent bond and other chemical bonds) via the atomic level potential energy and continuum mechanics. Furthermore, The Interfacial Element (TIE) has been introduced in CACM to bridge the interface of nano/bulk system, and with the capability of TIE, CACM should be able to tie nano and bulk (namely, local-global) structures seamless in one multi-scale system. Finally, atoms, super-atoms and continuum mechanics based finite elements all were connected in one micro-macro (namely, local-global) simulation model using minimum energy technology. A typical CACM modeling is treated as clustered beam element with characters of axial forces, bending moments and torsions. The stacking energy between adjacent base pairs is essentially van der Waal



force interaction which is described by the L-J potential form:

$$\phi(r_{ij}) = 4\varepsilon \left[ \left( \frac{\sigma}{r_{ij}} \right)^{12} - \left( \frac{\sigma}{r_{ij}} \right)^6 \right] \quad (21)$$

where  $\varepsilon$  is the depth of the potential well and  $\sigma$  is the (finite) distance at which the interparticle potential is zero and  $r$  is the distance between the particles.

The molecular bonds between pairs are mechanically transferred into bending moments and forces which are expressed as:

$$F_j = \sum_i C_{(j,i)} \frac{\partial}{\partial x_i} E(R_0 + dx_i, \theta_0 + d\theta_i) \quad (22)$$

where  $i, j$  and  $C_{(j,i)}$  represent the number of hydrogen bonds, different kinds of reaction forces/bending moments/torque and weighting coefficients. Note that  $x_j$  is displacement along the hydrogen bond direction.  $\theta_j$  is the angle change between donor and acceptor, and  $\theta_j = f_j(dx)$ , where  $f$  is the specific function with respect to  $j$ . From theoretical, simulation results and computational efficiency aspects, CACM method can provide a feasible simulation technique to bridge the gap of atomistic and continuum mechanics. The CACM, an energy-based numerical analysis/prediction method adopted in this project is very flexible, effective, and robust, it is able to handle multi-scale, multi-loading simulation and process modeling applications which is not possible for any other existing methods.

### 3. Results and Discussion

#### 3.1 NCD deposition

##### ***3.1.1– Characterizing the effect of surface pre-treatment on seeding of flat surfaces and highly curved tips***

Silicon wafers were seeded with nano-diamond particles prior to film growth to provide nucleation sites for diamond growth. To study the effect of surface treatment on the dispersion of the seeding, both Piranha cleaned and as received silicon wafers were seeded. The wafers seeded after Piranha cleaning show non-uniform dispersion of seeds across the sample as shown from SEM images at two different magnifications for the same sample in Figs. 2a-b. Patches of densely packed seeds were observed but a large portion of the surface remains unseeded.

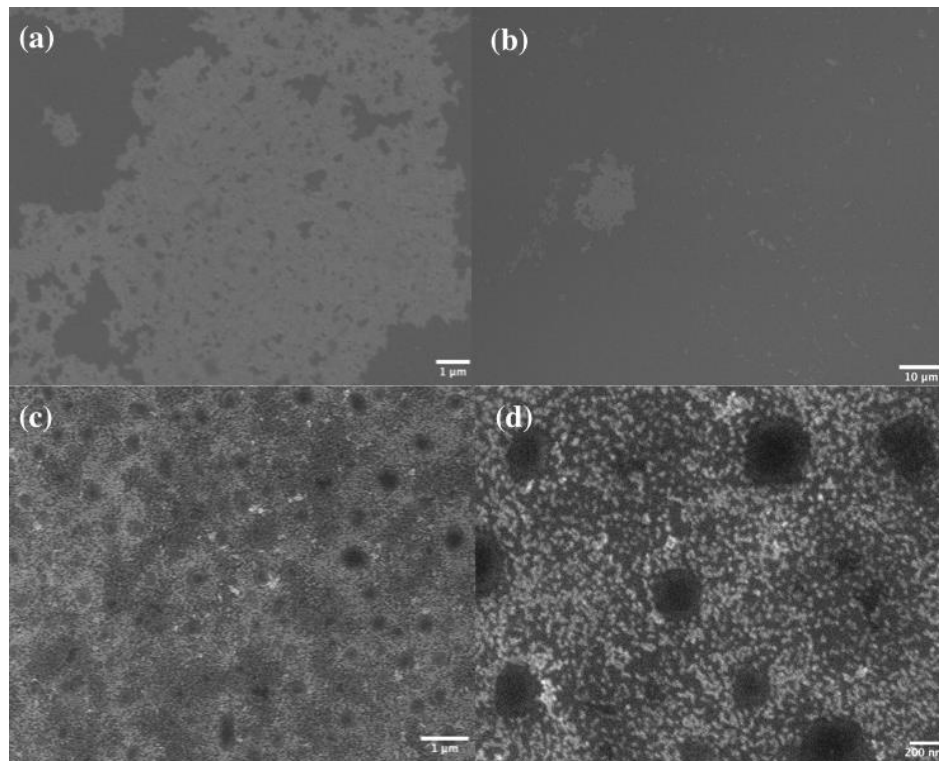


***Fig. 2: SEM images of silicon wafers seeded after Piranha cleaning (a-b) and after no Piranha cleaning (c-d).***

The as received sample shows uniform dispersion of the nano-diamond seeds across the sample as shown in Figs. 3c-d. For these samples, the seeds are densely packed and only small circular areas with no seeds are seen. Piranha cleaning of the silicon wafers makes surfaces highly hydrophilic thus resulting in dewetting of the multi-functionalized diamond seeds. As received silicon wafers are appropriate to generate uniform seeding.

AFM tips were seeded with nano-diamond particles prior to coating with NCD to provide nucleation sites for diamond growth during chemical vapor deposition. The effect of a 2 nm thick carbon coating, generated by sputter coating (Quorum, USA) as received AFM tips, on seed dispersion and later uniformity of NCD coatings on the tips was studied. The seed dispersion on the silicon tips without carbon pre-coat was non-uniform with many areas left unseeded; however, the tips with a carbon pre-coat show uniform dispersion of the seeds. Previous work has shown that a layer of carbon increases seed uniformity but the method of deposition shown in this study has not been reported [13]. The carbon coat increases the sticking coefficient of the substrate for the seeds and prevents carbon from dissolving in the silicon substrate for more uniform film growth [14]. To compare seeding with and without carburization on the same surface, only the area around tip as shown in Figs. 4 was covered with carbon layer using an SEM beam (applied beam voltage 7 kV) while the rest of the cantilever was left uncoated. After seeding, the area without carbon deposition shows non-uniform dispersion of seeds while the area with carburization shows a uniform spread.

To reduce the build-up of seeds seen in the previous samples, adjusted seeding procedures were tested with lower sonication times and higher nano-diamond seed dilutions in methanol. Fig. 5 a shows a sonication time of 10 minutes with nearly no build-up of seeds at the tip. As we increase sonication time to 20 minutes, a small build-up of seeds at the tip can be seen. Even more build-up of seeding at the tip results from a higher dilution of seeding during a 20-minute sonication period. Therefore, a sonication time between 10 and 20 minutes with the lower dilution is sufficient to disperse the seeds on the tip with little to no build-up.

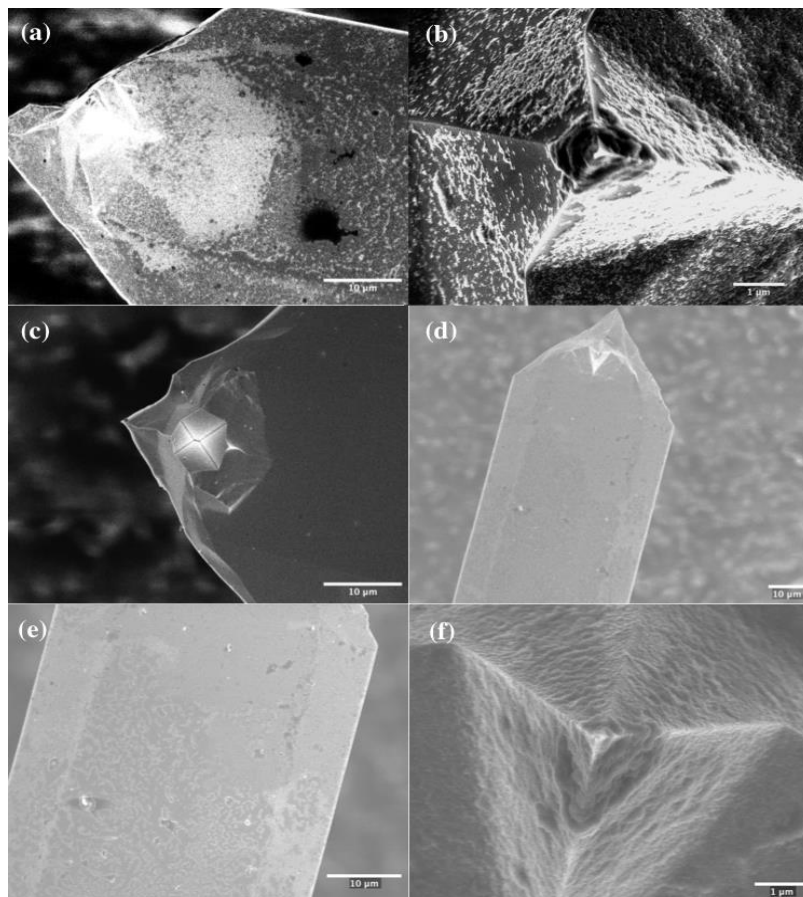


**Fig. 3: SEM images of seeded AFM tips without a carbon layer deposited before seeding (a-b) and with a carbon layer deposited before seeding (d-f) on area of the tip shown in (c).**

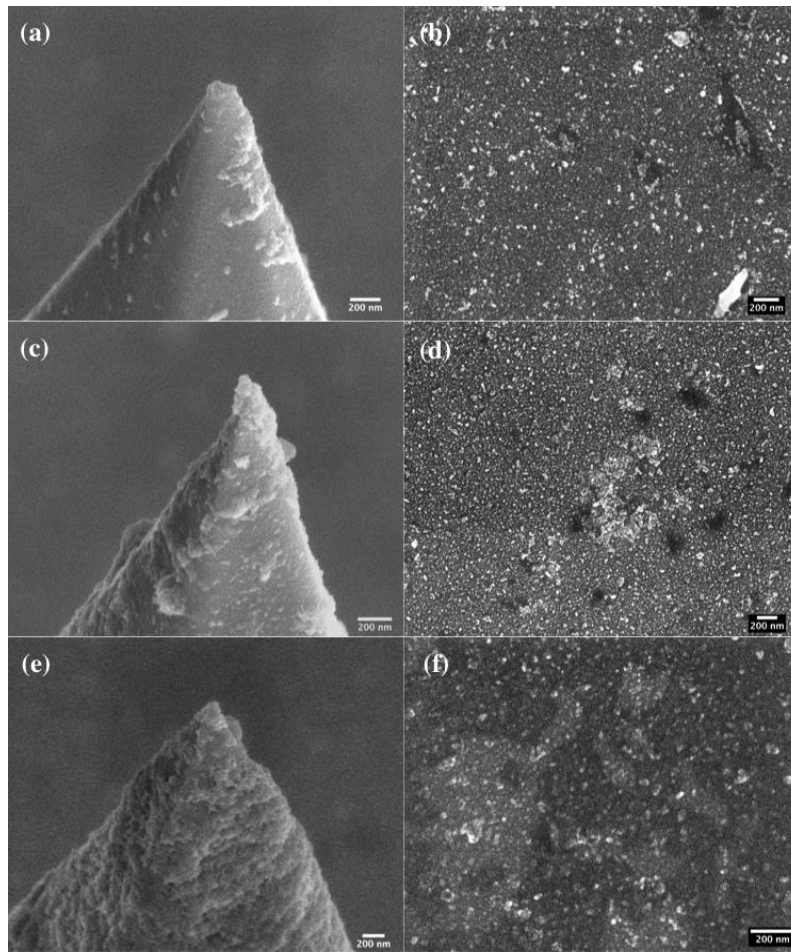


**Fig. 4: SEM images of AFM tips with carbon layer deposited by sputter coating before seeding in a seed dilution of 1:5 in methanol for a 10-minute sonication period (a-b) and 20-minute sonication period (c-d). Tips seeded in a higher seed dilution of 1:10 in methanol for 20-minute sonication time (e-f) were also tested.**

### **3.3.2 – Characterizing the roughness of NCD grown on flat surfaces and highly curved tips.**

Deposition parameters for high quality growth of NCD films via HFCVD were first optimized by characterizing the films on flat silicon substrates and later used to coat AFM tips. Pressure, temperature, methane concentration, and time were optimized to produce uniform coatings with low surface roughness and grains less than 50 nm. To study the effect of methane concentration on the roughness of NCD films, films were grown on seeded silicon wafers for 2 hours at 30 mbar with methane concentrations ranging from 3-5 vol% in hydrogen. Fig. 6 shows the methane concentration of 4 vol% comparatively gives lower roughness for the NCD films grown and thus is selected for the remainder of the study. This concentration has also been reported as an optimum value for deposition in literature for successful NCD film growth [15, 16].

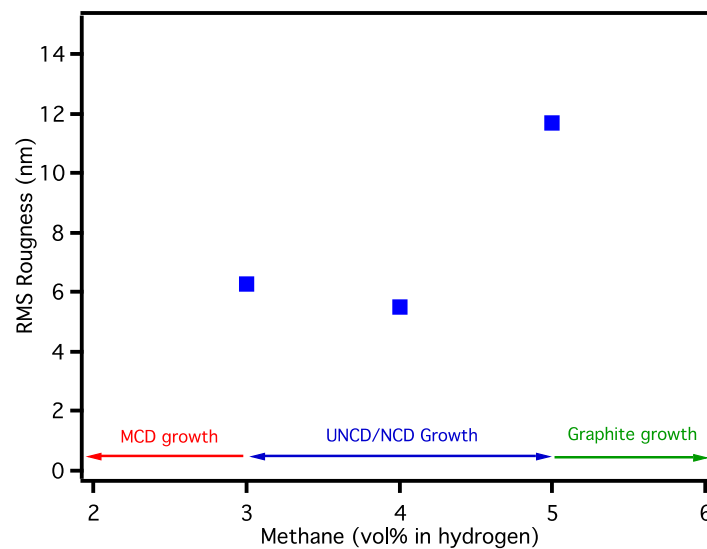


**Fig. 5: Roughness values measured from topographical images acquired using AFM show 4% methane produces the lowest roughness on flat wafers.**

The effect of pressure (30 and 50 mbar) on the coating uniformity was also tested. Since coating uniformity is most important on the AFM tip, this study was conducted for tips only. Fig. 6 shows that the coatings produced at 50 mbar are non-uniform with high roughness while the coatings produced at 30 mbar are uniform with lower roughness. Therefore, a pressure of 30 mbar is used for the remainder of the coatings in the study.

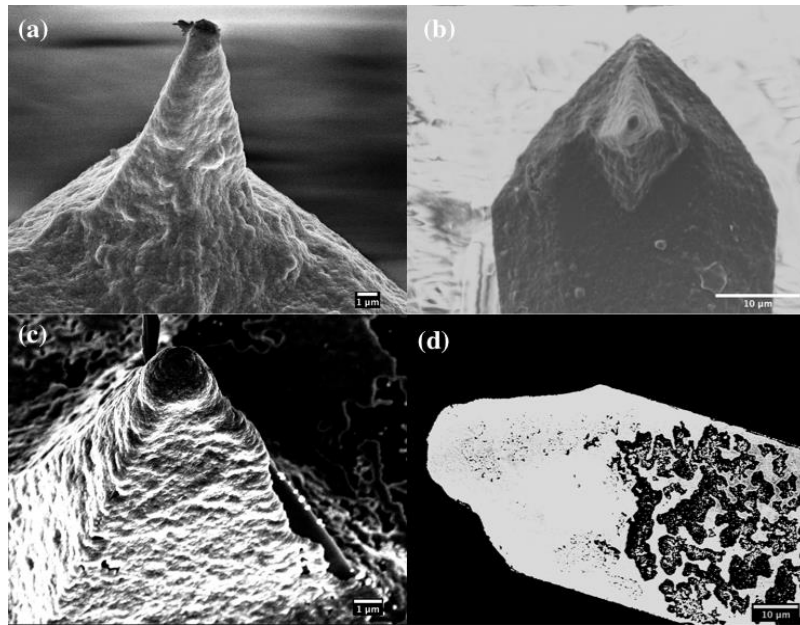


**Fig. 6: SEM images of NCD-coated tips grown for 1 hour under 4% methane at 30 mbar (a-b) and 50 mbar (c-d)**

The effect of the filament temperature on the film growth was studied for temperature ranges: 1200-1500°C and 1600-1800°C. The properties of the films grown at lower temperatures shown in Figs. 7a-b show unexpected film growth trends and produce grain sizes near 100 nm for deposition times ranging from 1 to 4 hours. However, at higher filament temperatures in Figs. 7c-d, the films follow expected growth trends, exhibit lower grain sizes, and are more uniform. Higher temperatures lead to increased concentration of radicalized methane and hydrogen ions for faster diffusion of the gases to the

substrate and therefore, produce higher growth kinetics and uniform NCD deposition [17]. The higher temperature growth profile shows linear behavior and predicts a film growth rate of 100 nm/hr. The average grain sizes are well below 50 nm and the surface roughness remains less than 10 nm for deposition times of 0.5 – 2 hours. Surface roughness less than 10 nm and grain sizes less than 50 nm are excellent for coatings that will be used on AFM tips for nanolithography applications. For this reason, a higher filament temperature is maintained for the remainder of the study to produce NCD films.

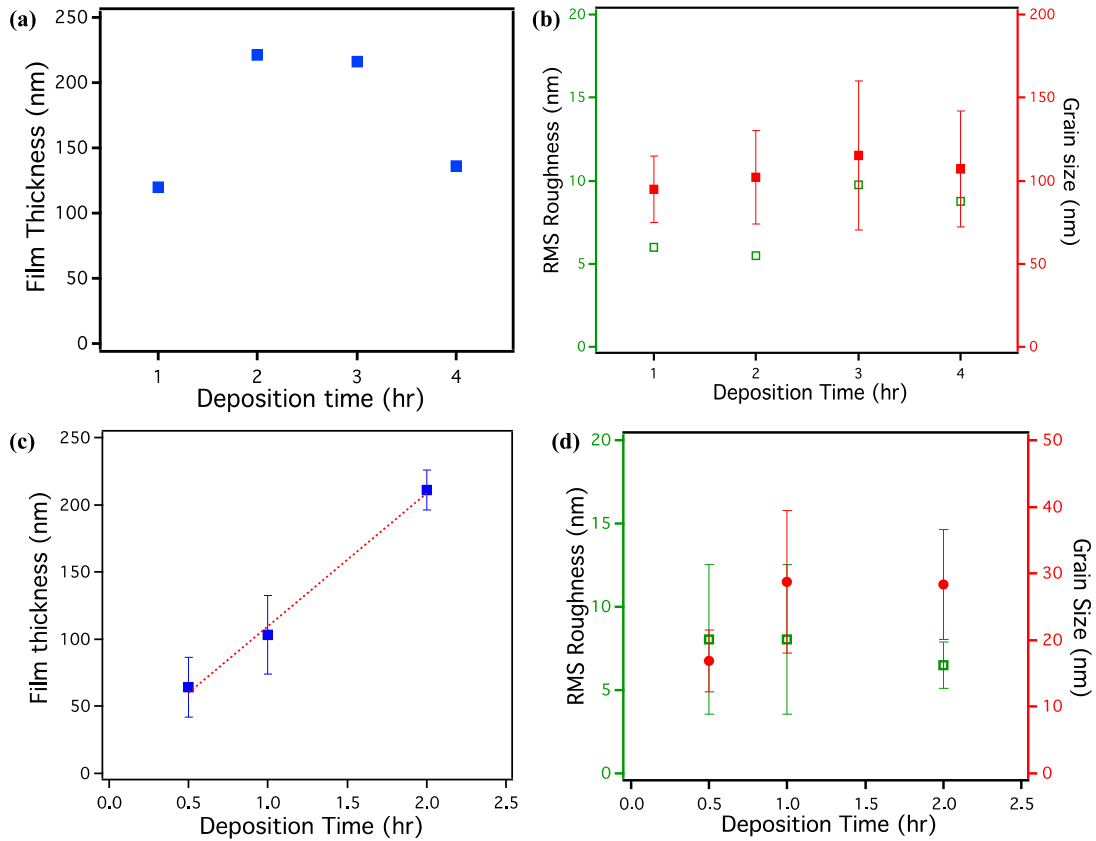


**Fig. 7: Film kinetics, measured by Zygo, show inconsistent growth trends at low temperature (a) and average grain sizes (red filled circles), measured by SEM shown, of nearly 100 nm for growth times ranging from 1-4 hours (b) while at higher temperatures the kinetics show a linear trend (c). The roughness (green open squares), measured by AFM, and grain sizes produced at higher temperatures are sufficiently sized for NCD coatings on a nanolithography tool (d).**



### 3.3.3 – Characterizing the NCD films using Raman, XPS, and NEXAFS

Raman spectroscopy was performed on NCD films grown on silicon wafers (30 mbar and 4% methane) to qualitatively estimate the film thickness of the NCD films for deposition times ranging from 0.5 – 2 hours. The spectra also indicate the presence of both  $sp^2$  and  $sp^3$  in the NCD film. Table 1 lists the characteristic NCD peaks exhibited by the spectra in Fig. 8. As the deposition time increases from 30 minutes to 2 hours, the ratio of  $SiO_2$ /NCD region in Table 2 reduces to indicate a linear increase in the film thickness of NCD films, in agreement with film thickness measurements from Zygo in Fig. 7a. Also, the crystalline diamond peak at  $1334\text{ cm}^{-1}$  diminishes with increase in deposition time, which indicates smaller  $sp^3$  grains surrounded by  $sp^2$  boundaries [13].

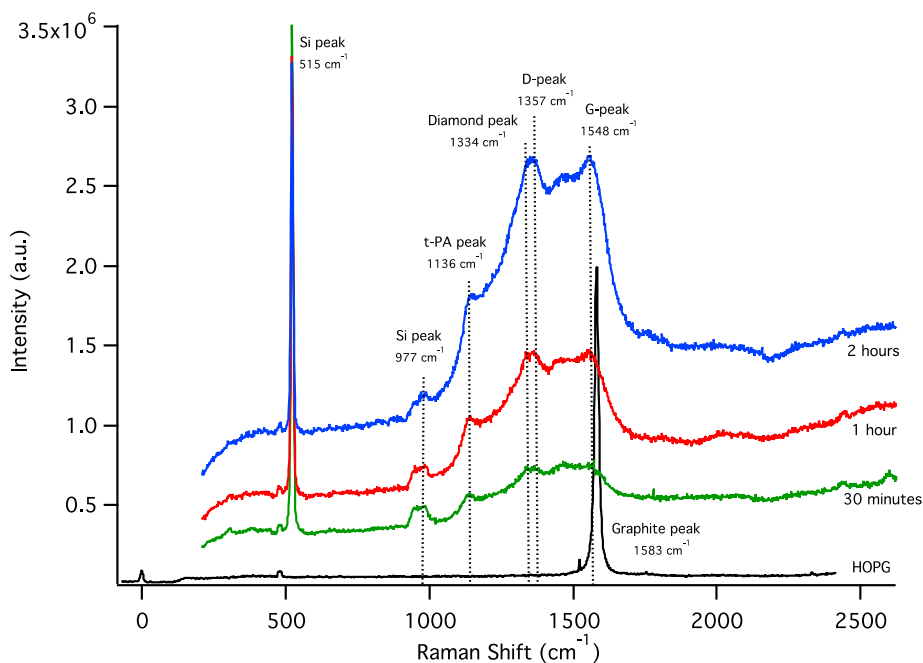


**Fig. 8: Raman spectra of films grown on silicon wafers at 30 mbar and 4% methane for 30 minutes, 1 hour, and 2 hours show peaks characteristic of NCD.**

**Table 1. Raman peaks exhibited by NCD films grown at 30 mbar under 4% methane for 0.5–2 hours**

Raman Shift (cm <sup>-1</sup> )	Peak Assignment
515, 977	Silicon
1136	Trans-poly(acetylene) at grain boundaries
1334	Crystalline diamond
1357,1548	D and G bands of fine crystal carbon

**Table 2. SiO<sub>2</sub>/NCD area from peak fitting of Raman spectra in Fig. 8**

Deposition Time (hr)	SiO <sub>2</sub> Area (x10 <sup>7</sup> )	NCD Area (x10 <sup>7</sup> )	SiO <sub>2</sub> /NCD
0.5	3.03	9.64	0.31
1	2.62	24.1	0.11
2	2.15	49.3	0.04

NEXAFS was also performed on NCD films grown on silicon wafers (30 mbar and 4% methane) for deposition times of 1 and 3 hours to quantitatively determine the fraction of sp<sup>2</sup> phase present in the film and to check for fluorine and oxygen contaminations. The fraction of sp<sup>2</sup> in the samples, calculated from the ratio of sp<sup>2</sup>/sp<sup>3</sup> peak intensities in the spectra in Fig. 9a, is 2±1% for both samples. The spectrum in Fig. 9b indicates a small oxygen contamination in the samples by the presence of the peak at 543 eV in the oxygen K-edge spectra. This surface oxidation occurs when NCD is stored in air prior to measurement. Fluorine contamination was previously found in NCD coatings produced in the same HFCVD chamber due to oil leakage from the pump. However, after cleaning the chambers thoroughly, backing the chamber and conducting numerous coatings in presence of reactive hydrogen, no fluorine signal is detected as shown by the lack of signal in the fluorine K-edge spectrum in Fig. 9c. Now, high quality coatings are generated with very low percentages of graphitic phases and no fluorine contamination.

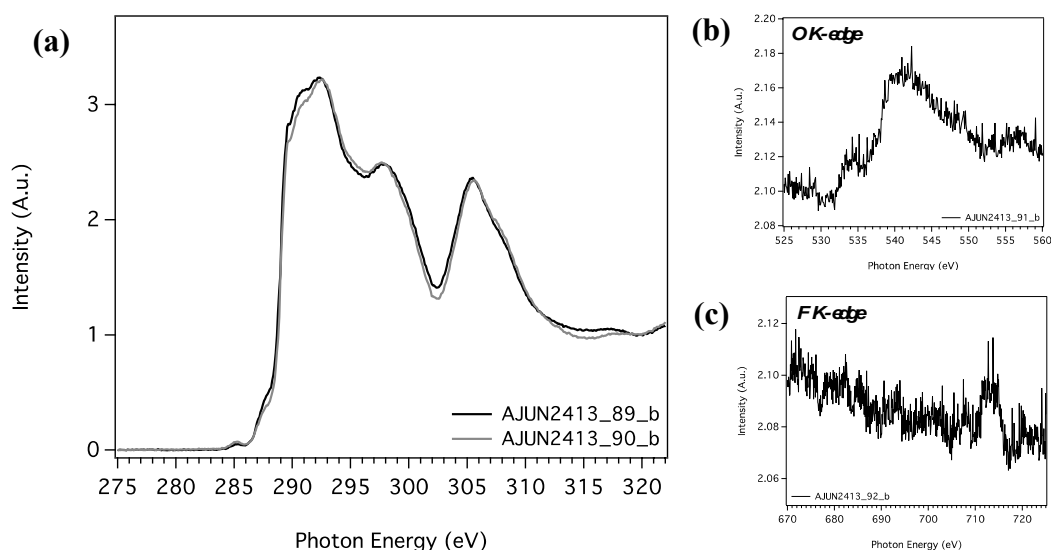


**Fig. 9: NEXAFS spectra of films grown on silicon wafers at 30 mbar and 4% methane for 1 and 3 hours show characteristic peaks of NCD (a). Surface oxidation is seen (b) but no fluorine contamination is detected (c).**

XPS was performed on NCD film (30 mbar under 4% methane for 30 minutes) to determine the surface layer chemistry. The sample was held under nitrogen after deposition until the time of measurement to prevent oxidation of the surface as seen for the NEXAFS samples that were stored in air. The lack of signal at the O 1s binding energy of 531 eV in Fig. 10 indicates no oxidation occurred on the film surface. The F 1s peak is not seen at 689 eV in good agreement with the NEXAFS results shown above. The C 1s peak of carbon at 284 eV tells us that carbon is arranged in a diamond structure and the signals just above 300 eV are characteristic of bulk and surface diamond plasmon signals that are commonly seen in diamond films. [14].

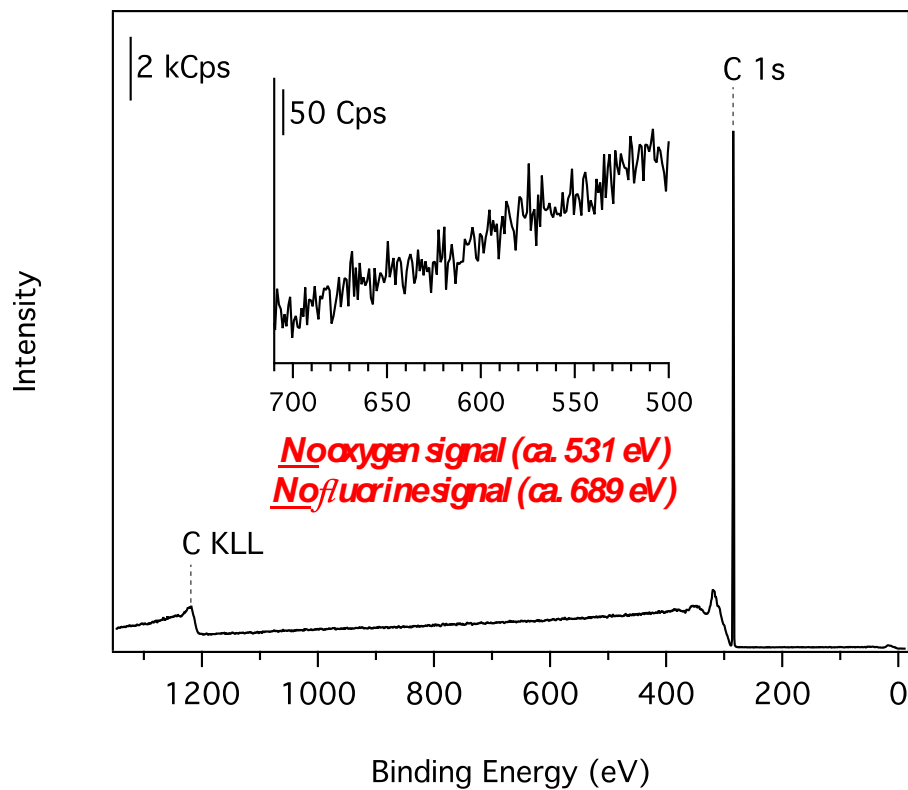


**Fig. 10: The XPS spectra of a film grown on a silicon wafer at 30 mbar and 4% methane for 1 hour indicates the film contains carbon in a diamond structure with no surface contaminations from neither oxygen nor fluorine.**

The Raman spectroscopy, NEXAFS, and XPS results confirm that films grown under 30 mbar with 4% methane for deposition times ranging from 30 minutes to 2 hours have a structure characteristic of NCD. Fluorine contamination is no longer present in the samples and no oxidation occurs if the films are stored under nitrogen atmosphere. The purity of the sample helps retain the hydrogen termination for effective chemical functionalization, which will be discussed in section 2.5. Chemical functionalization of AFM tips will be an active area of study for the future of this project.

### **3.3.4 – Growing NCD on probe tips**

To achieve high quality coatings on AFM tips, the tips were sputter coated with a thin carbon layer before seeding. The optimized parameters as indicated in the above section were used for NCD growth on a tip. The sputter-coated tips produced uniform coatings, but in few cases, a build-up of NCD film is seen at or near the tip. To avoid such a build-up and to keep a sharp tip, for high-resolution nanolithography, NCD growth was performed on tips with lower sonication times during seeding whose procedure is detailed in section 2.2. Fig. 11 shows the NCD coating produced on the tips seeded for 10 and 20-minute sonication periods have little build-up of NCD at the tip. Magnified views of the NCD grains show grain sizes less than 100 nm and reverse imaging of the tips, using AFM, on a regularly grained NCD surface estimates tip radius of 250-500 nm. Wear-resistant NCD-coated AFM tips with low surface roughness and nano-sized grains are successfully generated by HFCVD growth at 30 mbar with 4% methane. The radius of curvature and the uniform coating (25 nm thickness) are sufficiently sized for high-resolution nanolithography with these tips.

As a test to see if the NCD surface is reactive with chemical groups known to react with diamond, a NCD-coated silicon wafer (30 mbar at 4% methane atmosphere for 1 hour) was hydrogen terminated and then reacted with undecylenic acid (UA), a molecule whose terminal alkene group reacts with C-H bonds to form covalent C-C linkages. FTIR spectroscopy was performed to confirm the covalent bonding of the UA to the NCD coating. Fig. 12 shows the spectrum of a UA-NCD coating with a hydrogen terminated NCD as the subtracted background. The peak at  $1711\text{ cm}^{-1}$  indicates the

presence of the C=O of a carboxylic acid, indicating that UA has attached to the NCD. Additionally, the peaks at 2930 and 2852  $\text{cm}^{-1}$  are assigned to the  $\text{CH}_2$  stretching of the UA carbon chain and the peak at 1469  $\text{cm}^{-1}$  is assigned to the  $\text{CH}_2$  scissoring of the UA. The small peak at 1432  $\text{cm}^{-1}$  is indicative of the C-O-H stretch in the carboxylic acid and the peak at 1270  $\text{cm}^{-1}$  shows the C-O stretch of the acid [15].

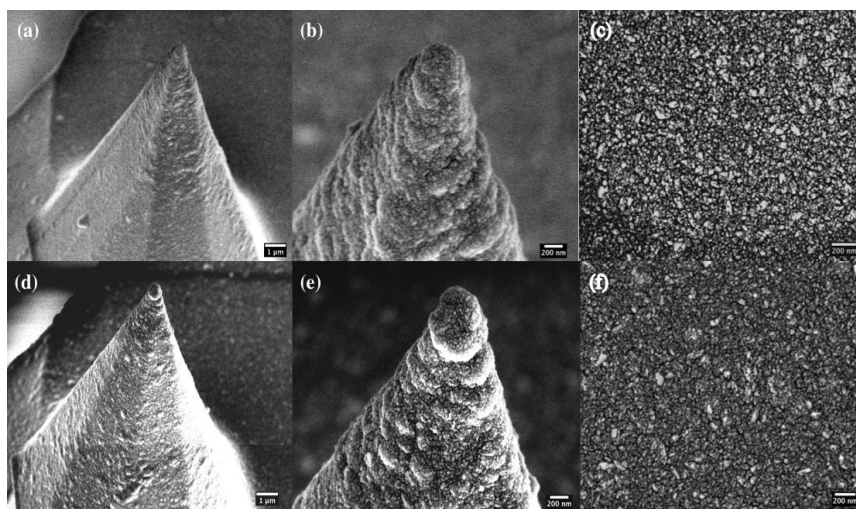


**Fig. 11: SEM images of NCD-coating grown for 15 minutes at 30 mbar and 4% methane on AFM tips after sonication in 1:5 dilution in methanol for sonication time of 10 minutes (a-c) and 20 minutes (d-f).**

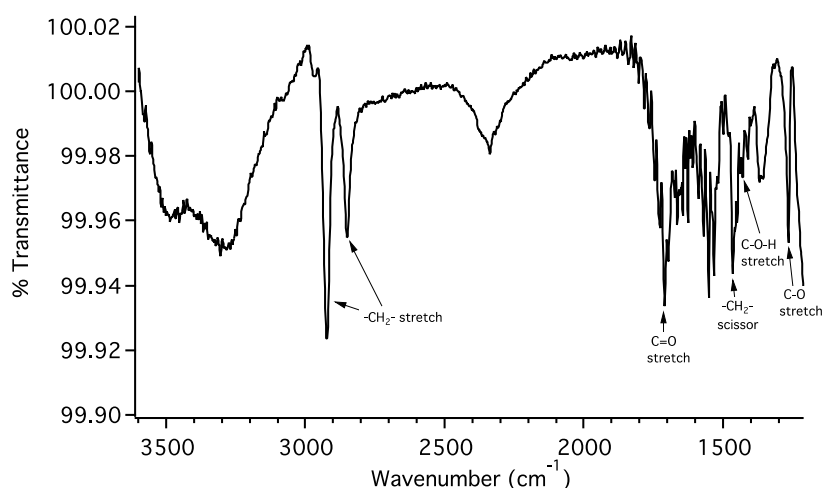


**Fig. 12: FTIR spectrum of UA-NCD film with hydrogen terminated NCD as background shows peaks characteristic of the carboxylic acid of UA and confirm the attachment of UA to hydrogen terminated NCD.**

### 3.2 Assessing the properties of *conductive* UNCD

The high hardness, modulus, and wear resistance of NCD and UNCD make them desirable for a wide variety of micro- and nano-scale applications; however, their low electrical conductivity preclude their use in many functional devices. It has been previously shown that by doping with Boron (at a concentration of X ppm), both types of films can achieve metallic conductivity and even superconductivity under certain conditions. Further, by bringing the deposition temperature down to 450°C, conductive NCD and UNCD can be made fully compatible with existing CMOS fabrication processes. While there has been extensive electrical characterization of these conductive films, there has been little investigation of the effect on structure and mechanical properties of the Boron-doping. Below, we have used NEX-AFS, high-resolution TEM, and nanoindentation to characterize and compare the different materials.

#### 3.2.1 *NEXAFS comparison of conductive and regular UNCD*

Synchrotron-based near-edge X-ray absorption fine structure (NEXAFS) spectroscopy, which is sensitive to the element oxidation state, hydrogenation, hybridization, and local ordering, was employed to gain insights into the bonding configuration of boron-doped UNCD. NEXAFS measurements were carried out at the National Synchrotron Light Source (NSLS) at Brookhaven National Laboratory (BNL). The NEXAFS spectrum of undoped UNCD, shown in **Error! Reference source not found.3a**, exhibits the characteristic features of diamond, namely the edge jump at ~289.0 eV, the exciton peak at ~289.3 eV, and the second band gap at ~302.5 eV. All

these features are due to the C 1s  $\rightarrow$   $\pi^*$  transition for ordered sp<sup>3</sup>-hybridized carbon-carbon bonds. Besides the characteristic peaks of diamond, a small absorption band at 285.0 eV, which can be assigned to the C 1s  $\rightarrow$   $\pi^*$  transition for disordered sp<sup>2</sup>-hybridized carbon-carbon bonds, was detected. The sources of this sp<sup>2</sup>-bonded carbon are surface contamination, surface reconstruction, and grain boundaries. The presence of a subtle shoulder at ~287.5 eV, which could be attributed to the C 1s  $\rightarrow$   $\pi^*$  transition for C-H bonds, indicates the hydrogen termination of the UNCD surface.

The characteristic NEXAFS spectrum of B-doped UNCD (grown at the same temperature of undoped UNCD, *i.e.*, 750-800°C. See **Error! Reference source not found.**3a exhibits all the characteristic diamond features listed above. Doping UNCD with boron did not affect the fraction of sp<sup>2</sup>-bonded carbon in the film, but resulted in a subtle change in the absorption C 1s  $\rightarrow$   $\pi^*$  transition for disordered sp<sup>2</sup>-hybridized carbon-carbon bonds: while in the case of undoped UNCD this feature is symmetric, upon boron-doping a second band appeared at lower photon energies. The detection of this second peak might be attributed to the presence of unoccupied gap states lying below the  $\pi^*$  band. The effect of deposition temperature on the local bonding configuration was also investigated by NEXAFS spectroscopy. The X-ray absorption spectra of B-doped UNCD grown at temperatures ranging from 460°C to 850°C show significant changes. In particular, the fraction of sp<sup>2</sup>-bonded carbon was found to decrease upon increasing the deposition temperature up to 800°C. For deposition temperatures above 800°C, the B-doped UNCD films contain significant fractions of sp<sup>2</sup>-hybridized carbon.



The deposition temperature was also found to affect the amount of hydrogen in the near-surface region: upon growing the films at lower temperatures (460-600°C), the amount of C-H bonds formed on the sample surface is higher than that present on the coatings deposited at higher temperatures.

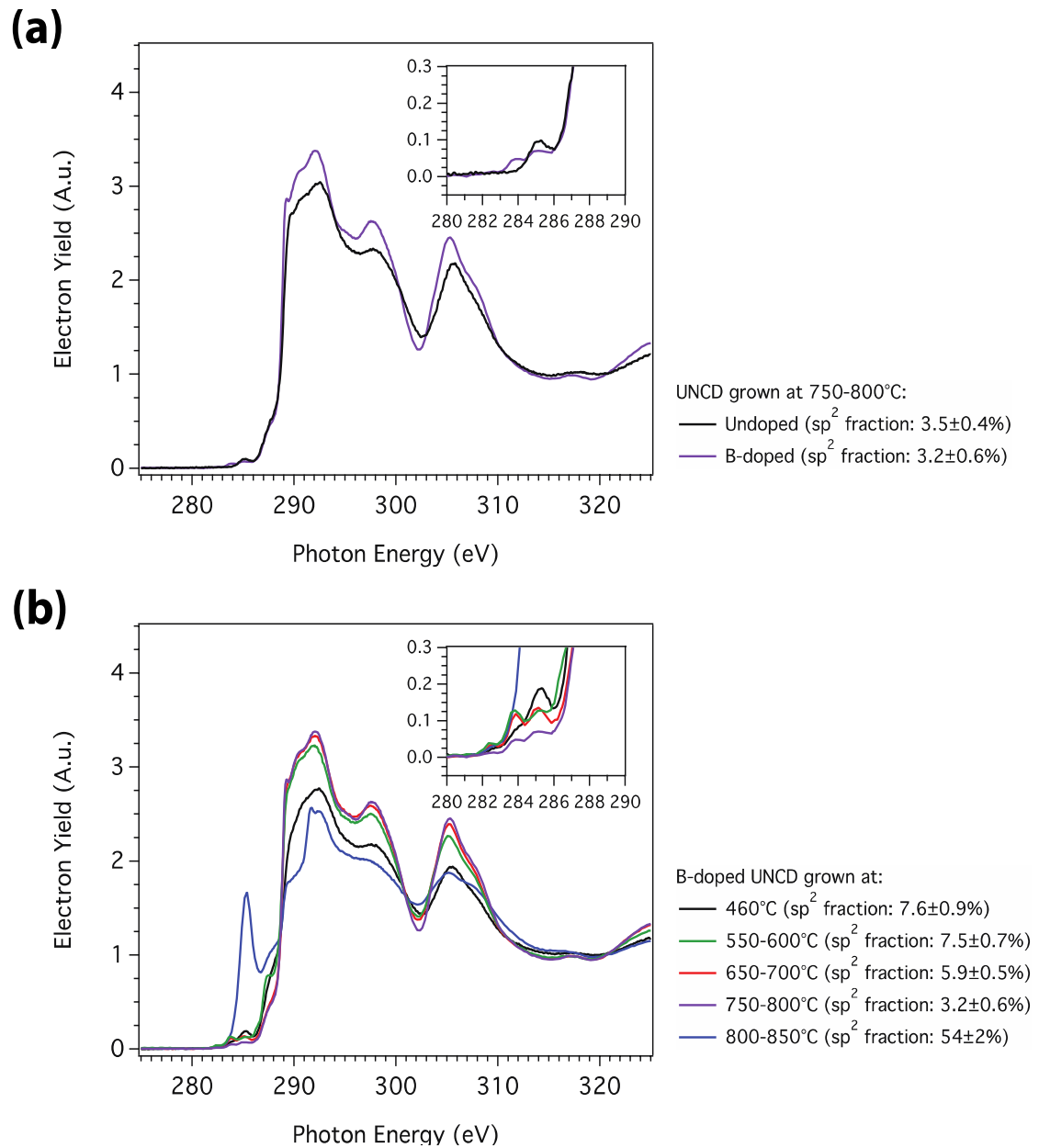


**Fig. 13: NEXAFS spectra of: a) undoped and B-doped UNCD grown at the same temperature (i.e., 750-800°C); b) boron-doped ultrananocrystalline diamond (B-UNCD) films grown at different temperatures. The fraction of  $sp^2$ -hybridized carbon is reported in the legend.**

### 3.2.2 TEM comparison of conductive and regular UNCD

Nominally identical AFM probes composed of regular (undoped) UNCD and conductive (B-doped) UNCD were compared using high-resolution TEM, as shown in Fig. 14. Other than the doping, the mold geometry and other conditions used to create the probes were identical. As is apparent from the imaging, the grain size of the B-doped probe was significantly smaller than the grain size of the undoped material. This result agrees with the XPS data showing a higher concentration of sp<sup>2</sup> carbon, since the in-grain material is almost exclusively sp<sup>3</sup> carbon, while the grain boundary material is a mix of sp<sup>2</sup> and sp<sup>3</sup> carbon. In future work, more probes will be imaged and cross-sectional TEM will be used to get more statistics on grain size and to quantify the differences in size distribution.

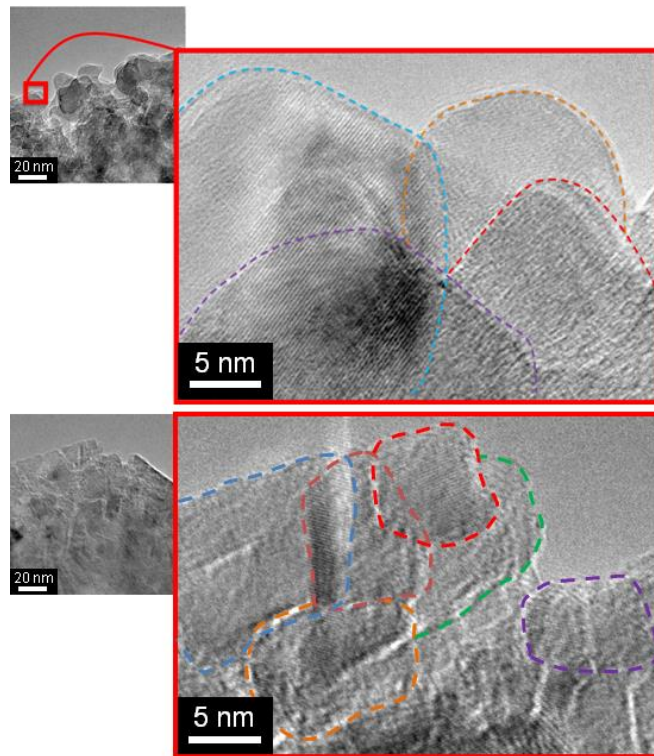


**Fig. 14: High-resolution TEM images of nominally-identical probes composed of regular, undoped UNCD (top) and of conductive, boron-doped UNCD (bottom).**

### 3.2.3 Comparison of mechanical properties using nanoindentation

A comparison was also made of the mechanical properties of conductive and regular UNCD. Films of regular undoped, B-doped, and low-temperature B-doped UNCD were deposited on silicon wafers. Nanoindentation testing was performed using a Hysitron Triboindenter, where nine different locations on each film. The averaged results are shown in Fig. 15. The elastic modulus values for undoped, B-doped, and low-temperature B-doped films were  $335\pm32$ ,  $287\pm40$ ,  $308\pm31$  GPa, respectively. The hardness values for the same three films were  $54\pm9$ ,  $52\pm2$ ,  $47\pm9$  GPa, respectively. All of these are within the statistical noise of the data. These results demonstrate that the B-doping has little effect on the desirable mechanical properties of UNCD.

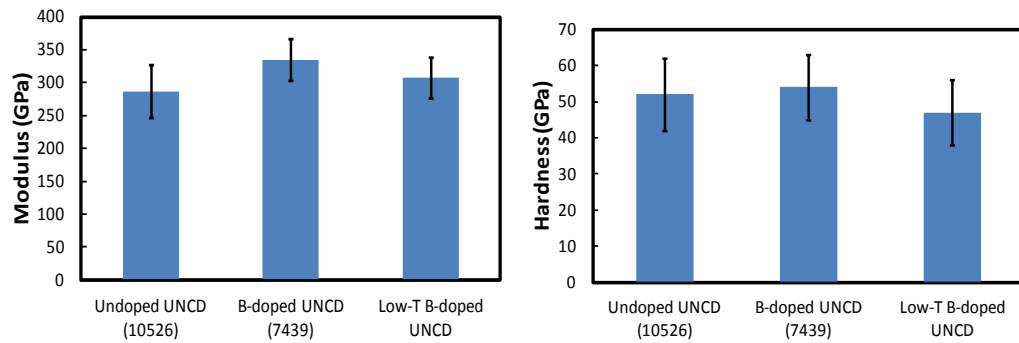


**Fig. 15: Nanoindentation was performed on regular, conductive, and low-temperature conductive UNCD films. The measured hardness and modulus are statistically equivalent for all materials.**

### **3.3 Assessing the significant impact of roughness on adhesion using in situ TEM adhesion tests:**

#### ***3.3.1 – Instrumentation for in situ TEM testing***

Two TEM systems have been used for the research at U. Penn. The first is a JEOL 2010F Field-Emission TEM/STEM. This is a state-of-the-art field emission transmission electron microscope with capabilities ranging from nanobeam and convergent beam diffraction to high resolution phase contrast, analytical and energy filtered imaging. The 2010F has been optimized for analytical microscopy with a large solid angle for high X-ray throughput, scanning, scanning-transmission, and backscattered electron detectors and a Gatan image filter for energy filtered imaging and electron energy loss spectroscopy. This combination of analytical capabilities makes the 2010F ideal for the characterization of a wide array of samples, but it is also a very capable high-resolution instrument with a point-to-point resolution of 0.23 nm. The second TEM at U. Penn is a JEOL 2010 TEM, available for both conventional and high resolution TEM imaging. It is equipped with single tilt, double-tilt, heating and cooling sample holders for a wide range of imaging experiments. The analytical objective lens pole piece on this microscope allows for sample tilting up to 45 degrees, while maintaining a point-to-point resolution of 0.25 nm. In addition to the conventional plate camera, this instrument is equipped with a Gatan Peltier cooled CCD imaging system for high quality digital imaging.

Nanoscale wear tests were conducted inside either the JEOL 2010F transmission electron microscope (TEM) at U. Penn, or inside a JEOL TEM at

CCU, using an in situ nanoindentation apparatus (PI-95, Hysitron, Minneapolis, MN). The in situ testing apparatus is shown in Fig. 16. A nominally flat (100)-oriented diamond punch was brought into contact with a series of sharp ( $R < 100$  nm) asperities (single crystal silicon, initially terminated with silicon oxide, or UNCD). The Si tips were model PPP-CONTR, (Nanosensors, Neuchatel, Switzerland), and the UNCD tips were custom probes provided by ADT, Inc. The tips were formed by coating commercial Si cantilevers with a UNCD film. Since the asperities are comprised of the ends of AFM tips which are integrated with microcantilevers, the cantilever deflection allows us to sensitively measure the applied force. Once in contact with a given tip, the diamond was then slid laterally, with reciprocating strokes typically of 100 nm, with only the adhesive force acting (no additional applied load). The contact was separated at varying intervals throughout the wear test to measure the instantaneous adhesive force, determined by observing the tensile deflection of the calibrated cantilever upon separation. Tips of varying shape were tested, with total sliding distances ranging from 200 nm to a few  $\mu\text{m}$  for each test. All sliding was recorded with real-time video, and high resolution (lattice-resolved, when possible) TEM images of the asperities were taken upon each separation. In post-processing, the instantaneous asperity profile was traced using the out-of-contact images. Then the profiles were integrated to three-dimensional shapes (assuming axisymmetry of each differential slice) to quantify the volume removed - and thus the number of atoms removed.

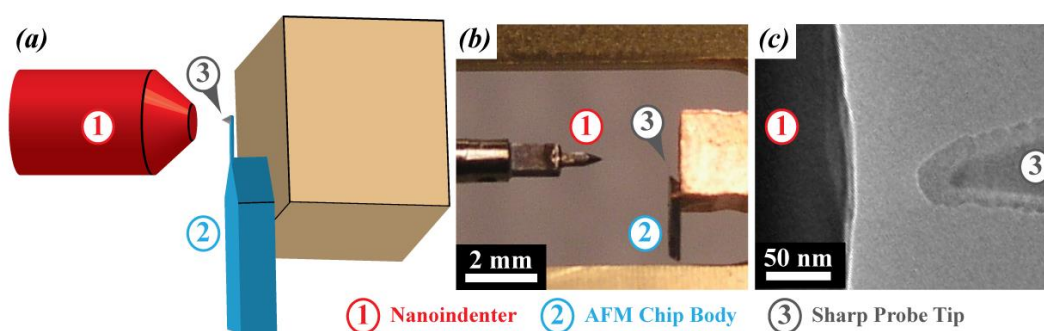


**Fig. 16:** A schematic of the *in situ* TEM experimental test setup is shown in (a). The actual apparatus is shown using a digital camera (b) and low-resolution TEM imaging (c). The relevant components are indicated using numbers corresponding to the legend shown.

### 3.3.2 – Measuring the effect of roughness on adhesion

The effect of atomic-scale roughness on adhesion of UNCD and diamond-like carbon (DLC) was examined using the *in situ* TEM techniques described above and also using atomistic simulations. Nanoscale UNCD asperities were brought into contact and then separated from single-crystal diamond surfaces inside the TEM. This allowed for characterization of the roughness of the sharp nanoasperities immediately before and after contact down to the Angstrom-scale. Analogous experiments were conducted using MD simulations. The root mean square roughness for the simulated tips spanned 0.03 nm (atomic corrugation) to 0.12 nm; for the experimental tips, the range was 0.18–1.58 nm. Over the tested range of roughness, the measured work of adhesion was found to decrease by more than an order of magnitude as the roughness increased (Fig. 17). The dependence of adhesion upon roughness was accurately described using a simple analytical model. This combination of simulation and experimental methodologies

allows for an exploration of an unprecedented range of tip sizes and length scales for roughness, while also verifying consistency of the results between the techniques.

Collectively, these results demonstrate the high sensitivity of adhesion to interfacial roughness down to the atomic limit. Furthermore, they indicate that care must be taken when attempting to extract work of adhesion values from experimental measurements of adhesion forces. These results were recently published in the journal Tribology Letters [16].

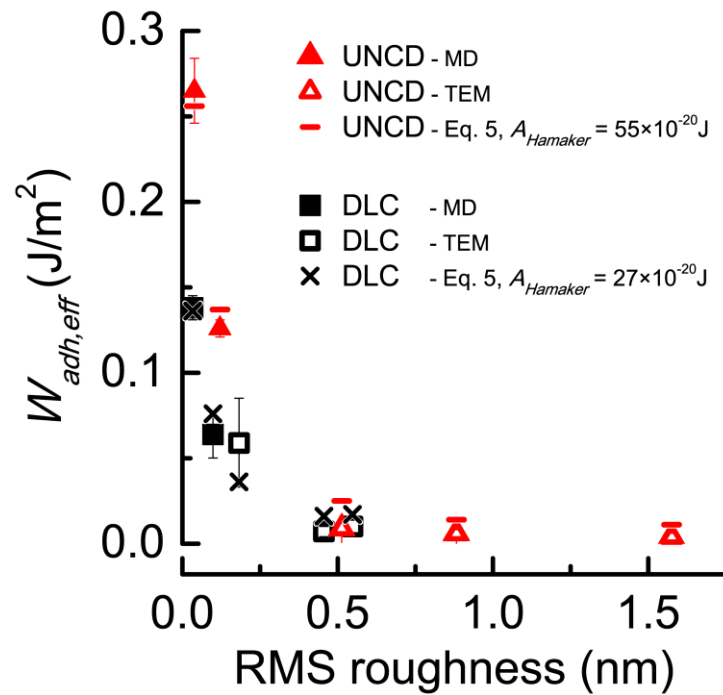


**Fig. 17: Demonstrating the effect of atomic-scale roughness on work of adhesion for UNCD and also DLC AFM probes pulling off of single-crystal diamond substrates. The results show an order-of-magnitude decrease in measured work of adhesion between the atomically smooth probes and those with just 5 Å of roughness. The data is well-fit by an analytical model based on van der Waals adhesion.**

### ***3.4 Demonstrating the wear resistance of UNCD probes using in situ TEM sliding tests***

In situ sliding wear tests were conducted at CCU during the visit by the U. Penn Ph.D. student and several others were conducted separately at each institution. During this visit, a number of skills were transferred between the CCU and Penn teams, including methodology for use of a Hysitron triboindenter, use of the in-site TEM PicoIndenter, use of the TEM itself, MATLAB scripts for data analysis, sample preparation methods, and various simulation and experimental methodologies relevant to the research program. The CCU TEM users were trained on use of specimen tilt, and given a brief tutorial on diffraction by the U. Penn team. Noise tests of the CCU PicoIndenter were also performed. The team found that the vibration amplitude of the PicoIndenter at CCU is on a par with the baseline noise observed in Penn's system. A mechanical system resonance exists at ~123 Hz, with an EMI peak observed at 120 Hz (2x line frequency). When the system is at rest, a standard deviation of position is observed to be 3 nm (measured at 1000 pts/s, with the instrument's "Qgain" setting set to 4). These are within the vendor's specifications for the instrument.

The team established a common procedure for TEM wear testing that involved initial imaging of probes via TEM, obtaining videos of approach/contact/retract measurements followed by imaging (usually capture 5-10 good pull-offs on video), and obtaining videos of sliding at adhesion-only loading (with higher resolution still images after each video). Images were obtained before sliding, and then after sliding distances of 200, 400, 800,



1600, 3200, and 6400 nm. Additional tests were performed by sliding under higher applied loads; analysis of this data is still in progress and so results reported here focus on the experiments performed under zero applied load. Results for one Si probe (tested at U. Penn), and two UNCD probes (tested at CCU) are shown in Fig. 18. The Si probe is seen to wear rapidly with each interval, while little wear of the UNCD probes is seen; the volume change is barely within the resolution limits of the technique. All three probes had comparable initial sizes.

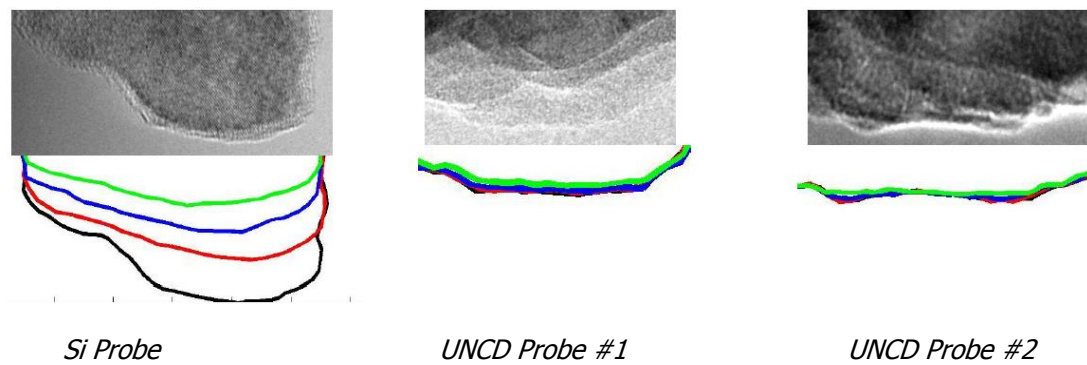


**Fig. 18: Top row: High resolution TEM images of the tested probes before any wear occurred. Bottom row: overlaid traces of the outer edge of the probes after sliding intervals of 200, 400, 800, 1600, 3200, and 6400 nm. The Si probe is seen to wear away rapidly, while barely any wear of the UNCD probe is observed.**

A plot of the worn volume vs. sliding distance is shown in Fig. 19. The plot shows quantitatively that the UNCD exhibits orders of magnitude less wear than the Si under comparable conditions. This agrees with our qualitative expectation that UNCD should exhibit less wear than Si at the nano scale, but provides unique and completely new quantitative data for such a comparison. Newer wear tests have been performed under applied loads of 300 nN, corresponding to initial stresses of more than 8 GPa. Initial data from these tests (illustrated in Fig. 20) demonstrates that wear can be

accelerated with high stress. Future work on this project will perform more high-load testing and analysis and investigate the kinetics of wear in UNCD.

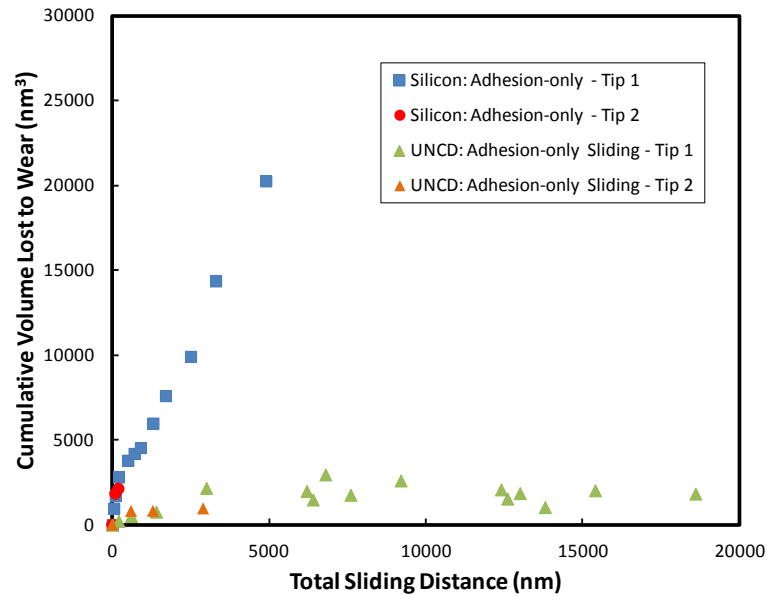


**Fig. 19:** A comparison of sliding wear for similar conditions of adhesion-only sliding for a standard silicon probes as compared to monolithic UNCD probes. The rate of volume lost (with sliding distance) is more than an order of magnitude smaller for UNCD.

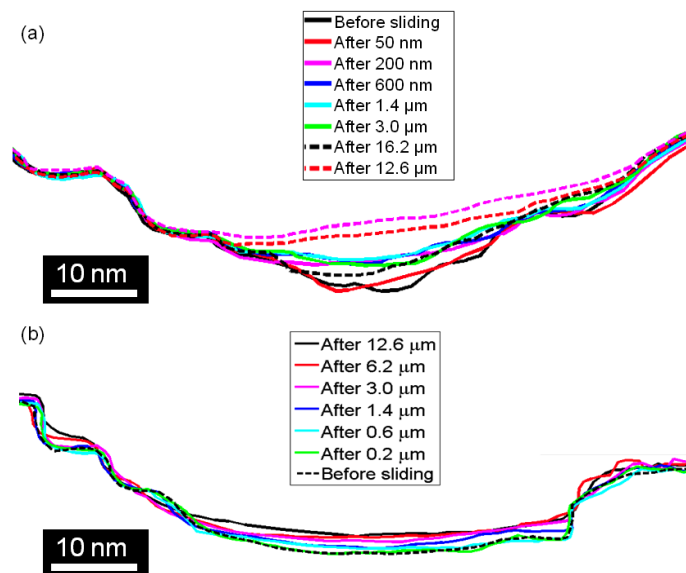


**Fig. 20:** Feasibility studies of high-load wear tests have been performed to accelerate wear of UNCD tips. Above are two different UNCD tips, each showing progressive wear after being subjected to sliding at high applied normal stresses. These results will enable comparison to models based on stress-mediated chemical kinetics.

### 3.5 Rehybridization due to sliding

We have also studied amorphization induced by frictional sliding. This work is a prelude to the main goal of looking at a nanoscale sliding interface between amorphous materials as a shear band, and also seeing if nanoscale lateral forces can induce shear transformation zone formation in the near-surface region of the material. We investigated deformation processes for tetrahedral amorphous carbon (ta-C), and propose that the sliding interface between two amorphous surfaces can be regarded as a shear band since it necessarily exhibits shear localization. A tribointerface is naturally weak, and correspondingly, we find a shear-band like localization of the strain in that region. In molecular dynamics (MD) simulations performed by collaborator M. Moseler, an a-C phase with low  $sp^3$  content is seen to form between ta-C/ta-C tribopairs. Interestingly, the a-C formation rate in the ta-C/a-C/ta-C system exceeds the amorphization rate in diamond/diamond tribopairs [17]. This is in excellent qualitative agreement with our NEXAFS analysis that suggests an enhanced a-C formation for the ta-C case compared to ultra nanocrystalline diamond (UNCD) [18, 19] (Fig. 21). Motivated by these observations, we choose the local hybridization, in particular the fraction of  $sp^3$  coordinated carbon atoms as an order parameter. The simulations show that a local coupling must be invalid for the particular case of ta-C. In particular, rehybridization precedes plastic events, and the materials needs to be weakened before it yields. This is possible because a large fraction of bonds in ta-C are severely pre-stressed in tension, and require only minute perturbation to break. This is in contrast to the behavior of diamond-diamond

tribopairs which show similar shear localization, but where the diamond to a-C transformation is confined to a region of low but finite shear rate (Fig. 22).

These results show that localized plastic events transform the surrounding material to a weaker state even in the presence of highly compressive external stresses. The non-local character of this process is in remarkable contrast to current models for plasticity in amorphous materials, but addresses the chicken-and-egg problem of whether plasticity causes changes in the order parameter field or vice-versa. While ta-C could be a special case, it is possible that other materials exhibit similar non-local behavior. The study of this particular phenomenon requires gradients in the order parameter field. Here, those were initially generated through the pairing of two distinct ta-C surfaces, but most computational studies of plasticity start from a homogeneous initial configuration in which it is difficult to disentangle non-local effects. This motivates further studies of amorphous interfaces. This work was published in Trib. Lett. [20].

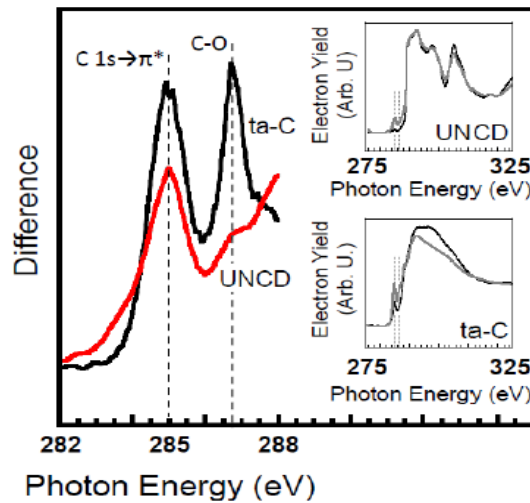


**Fig. 21: Difference in representative NEXAFS total electron yield spectra between worn and unworn regions of carbon-based films. Black curve: difference between a spectrum taken from a heavily worn (high load, low relative humidity) ta-C wear track and a spectrum from unworn ta-C. Red curve: difference between a spectrum taken from heavily worn UNCD and unworn UNCD. The upper inset shows the worn (gray) UNCD spectrum and the unworn (black) UNCD spectrum. The lower inset shows the worn (gray) ta-C spectrum and the unworn (black) ta-C spectrum.**

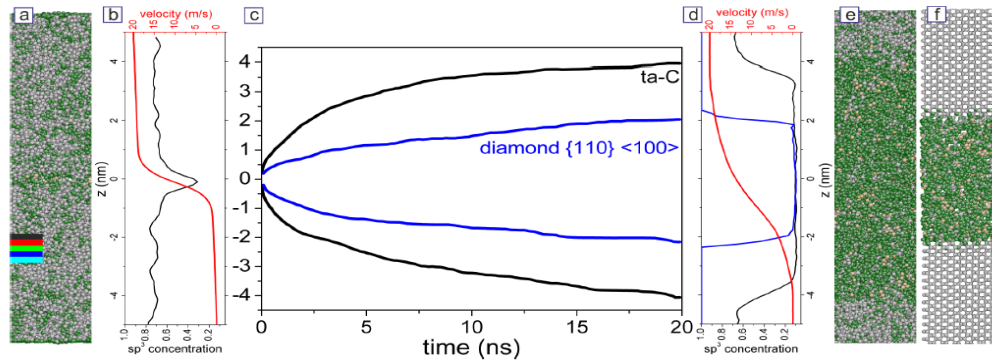


**Fig. 22: MD simulations from collaborator Moseler. (a) Snapshot of the ta-C/ta-C tribosystem after 0.1 ns of sliding. Atoms are color-coded according to their atomic coordination: white: 4-fold ( $sp^3$ ), green: 3-fold ( $sp^2$ ), yellow: 2-fold ( $sp^1$ ). The colored bars define layers that were used for further analyses in Fig. 3. (b)  $sp^3$  concentration (black curve) and velocity profile (red curve) across the ta-C/ta-C tribopair. (c) Evolution of the upper and lower boundary of the a-C tribofilm formed between two ta-C surfaces (black curve) compared to a corresponding film formed between two diamond (110) surfaces rubbed in  $\langle 001 \rangle$  direction (gray curve). (d)  $sp^3$  concentration (black curve for ta-C and gray curve for diamond) and velocity profile of the ta-C system (red curve) after 20 ns of sliding. (e) and (f) snapshot of the ta-C/ta-C and diamond/diamond tribosystems after 20 ns sliding.**

### 3.6 Atomistic simulations for contact behaviors and sliding mechanisms at nano-scale interfaces

#### 3.6.1– Effects of Absorbed layers on nanotribological properties of UNCD

Atomistic approaches and multi-scale simulations will be focused on nanostructure mechanisms and the interfacial phenomena to identify the key physical mechanisms that control friction and wear for sliding on UNCD, and to determine how these are affected by the mechanical properties, the film structure (H-content and grain boundary structure), and the surface chemistry at nano-, meso- and macro-scales. As shown in Fig. 23, the simulation model comprises a single crystalline of diamond, hydrogen adsorbed layers and a diamond indenter. The proposed model comprises three kinds of atoms, namely boundary, thermostat, and Newtonian. A periodic boundary condition is imposed on the diamond film to prevent the overflow of the hydrogen atoms in the adsorbed layer and serve to reduce the edge effects and to maintain the lattice symmetry. Meanwhile, the atoms next the periodic boundary are treated as thermostat atoms and are modified based on the Nose'-Hoover method [21] to drive the equilibrium temperature of the substrate toward the desired value.

#### **Wear test on UNCD thin films**

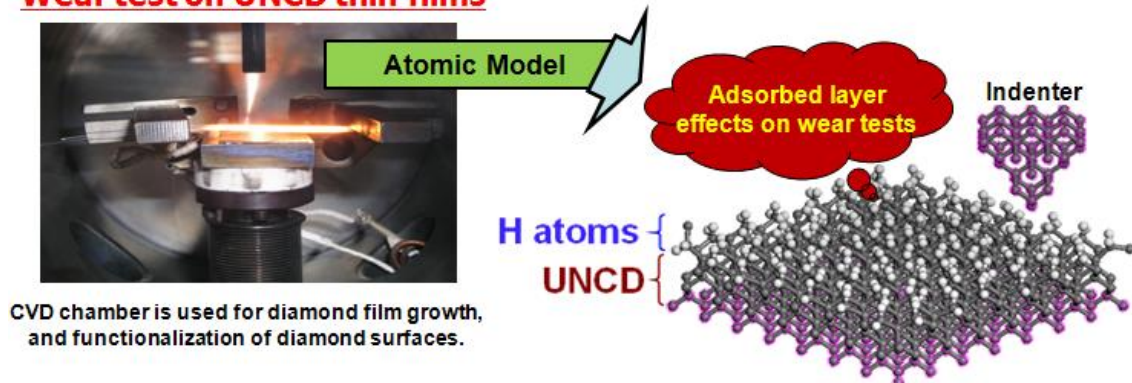


***Fig. 23: Initial simulation model for nanoindentation process showing diamond crystal slab, diamond indenter and hydrogen adsorbed layer.***

To further illustrate the effects of the adsorbed layer on the structural deformation of the diamond samples, Fig. 24 presents atomic configuration models which clearly show the formation of significant slip planes during the nanoscratch. Our results show the presence of slip planes aligned in the direction of the side faces of the pyramidal indenter. In general, as the indenter is pushed into the diamond sample, local polymer molecules become trapped at the indentation interface, thereby forming a cavity on the diamond surface. It is necessary to note that the diamond substrate and active adsorbed molecules react attractively via van der Waals interactions so that hydrogen molecules may penetrate into diamond substrate. Thus, the atomistic structure at the diamond surface can be changed depending upon the adsorption of surface species. A similar observation was also noted in the water effect on the deformation of silicon monocrystals by Tang and Zhang [22]. During the subsequent scratch stage, the hydrogen molecules remain trapped within the diamond substrate and thus the cavity grows, resulting in the formation of a rough residual depth and prompting the onset of slip planes along the edges of the indenter. However, when the substrate has no hydrogen adsorbed layer, the upper layer of the diamond substrate remains in constant contact with the indenter during nanoindentation. Following the scratch stage, the residual depth is found to have a relatively shallower penetration than that observed in the specimen with an adsorbed layer as a result of recrystallization and elastic recovery induced by the adhesion between the indenter and the diamond substrate. Note that these results are consistent with those reported by Luan and Robbins in their MD modeling of atomic contacts with and without adhesion, respectively [23]. Specifically, Fig.

24 reveals that the bonds between the C atoms in the diamond substrate and the C atoms in the indenter are weakened as a result of the hydrogen layers between them, and hence a poorer elastic recovery (i.e. attraction effects) takes place. In other words, the microstructural damage caused to the diamond substrate during the nanoindentation and nanoscratch becomes more severe as the adsorbed layer thickness increases. Overall, the results imply that the presence of an adsorbed layer reduces the mechanical strength of the indented specimen, particularly for indentation depth in the nanometer regime.

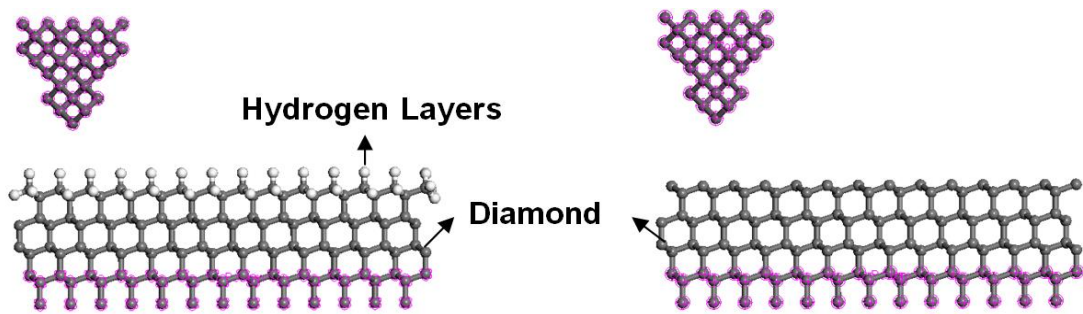


**Fig. 24: Atomic configuration of diamond substrate during nanoscratch tests: (a) with and (b) without hydrogen adsorbed layers, respectively.**

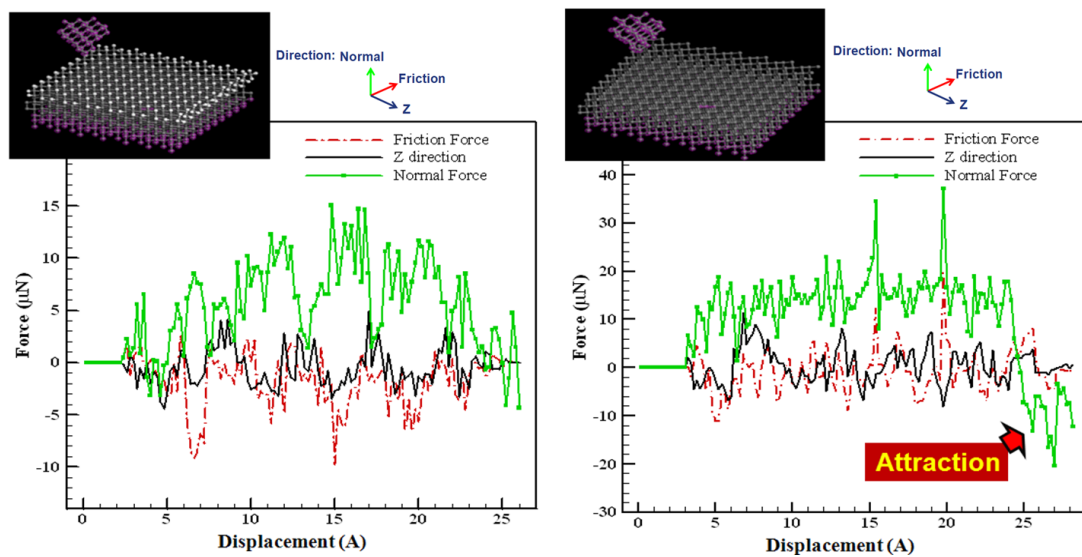


**Fig. 24: Variation of normal force, frictional force and lateral force to the sliding displacement for (a) with and (b) without hydrogen adsorbed layers, respectively.**



### 3.6.2–A Study on Lateral Junction Growth

Lateral junction growth at nano-scale is fundamental for the atomic origins of macroscopic friction and wear. Our present simulations also reveal that the lateral junction growth during incipient sliding coincides with the occurrence of dislocation in the junction. In this study, the model comprises three major components, namely a rigid carbon plate, a deformable copper asperity, and an adsorbed layer. In analyzing the junction growth mechanism, the slip vector analysis considers the  $\langle 1\ 1\ 1 \rangle$  slip plane of the f.c.c. copper lattice. In the simulations, fixed boundary conditions are imposed in the  $[1\ 0\ 0]$  and  $[0\ 1\ 0]$  directions, and the interactions between the carbon plate and the copper asperity are modeled using the Morse potential (See Fig. 25).

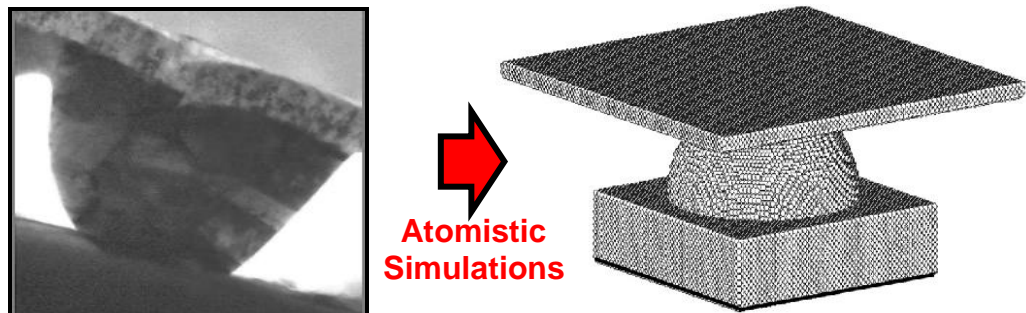


**Fig. 25: Atomistic configuration of simulation system comprising single copper asperity and flat carbon plate.**

Figs. 26 and 27 present the variations of the normal force acting on the flat, the lateral force acting on the asperity, the tangential force coefficient, and the lateral junction growth of the asperity contact, respectively, as the lateral displacement of the rigid flat is increased. Note that in Figs. 26 and 27, the notation “l 1” (for example) indicates a contact interference of 1 Å. As shown in Fig. 26, the normal force decreases smoothly as the flat is first displaced in the lateral direction, but then fluctuates periodically with a

sawtoothlike characteristic as the displacement is further increased. The reduction in the normal force during the initial stages of the sliding process can be attributed to slips of the asperity atoms, which lead to an increase in the contact area between the asperity and the flat [24]. Since the lateral displacement of the flat can cause the slips of asperity atoms that reduce the concentrated stress. As a result the normal force acting on the flat is decreased. A stepwise profile of each drop of normal force can be attributed to the occurrence of slips of asperity atoms. A more detailed description of the lateral junction growth mechanism can be found in the study of Jeng and Peng [24]. Our atomistic simulation demonstrates the characteristic fluctuations of force distribution during the lateral junction process from the atomic origins.

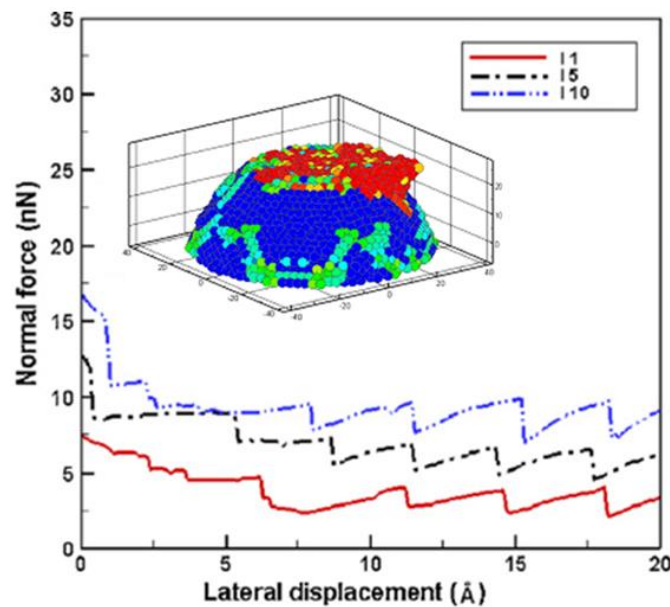


**Fig. 26: Normal force acting on flat plate as function of lateral displacement**

Fig. 27 shows that the lateral force increases initially with an increasing lateral displacement and then fluctuates periodically with a sawtooth-type profile; indicating the occurrence of a stick-slip phenomenon [25, 26]. From

inspection, the stick-slip pattern is found to repeat at an interval of around  $3 \text{ \AA}$ . According to the experimental findings presented by *Carpick et al.* [27], the period of the force fluctuation is roughly equivalent to the lattice spacing of single crystal copper. The displacement interval over which the lateral force increases continuously in Fig. 27 is roughly equivalent to that over which the normal force reduces in Fig. 26. It is reasonable, therefore, to infer that the transition point between the smoothly increasing region of the force curve and the periodically fluctuating region coincides with the point at which lateral junction growth ceases and is replaced by stick-slip motion [25-28]. The continuum mechanics study of Brizmer et al. [29] treated the sliding inception as a plastic yield failure mechanism to determine the ends of lateral junction growth. More recently, Wu and Adams [30] suggested that the adhesion can cause the load required to initiate plastic deformation to be far less than predicted by the Hertz contact [31]. The atomistic simulation conducted in this study intrinsically accounts for the effects of adhesion and facilitates the observation of slip of atoms, which is an indication of plasticity.

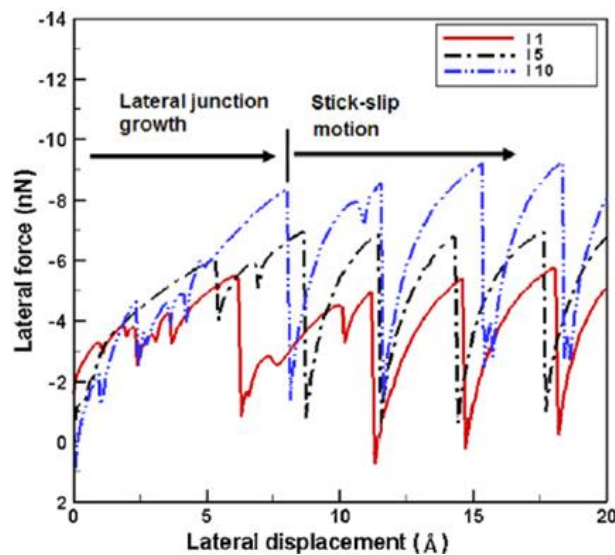


**Fig. 27: Lateral force acting on asperity as function of lateral displacement**

Fig. 28 shows the variation of the lateral junction growth as a function of the various angles at the similar contact interference for the cases without an absorbed layer. Here, the junction growth of various lateral displacement steps is calculated by the ratio of the current contact area to that at the beginning of lateral movement. Note that in computing the size of the junction, the boundary of the contact area is taken as the point at which the contact pressure reduces to zero [32]. The results show that for a constant value of the contact interference, the lateral junction growth increases with increasing sliding angles as the lateral displacement is increased. Therefore, the larger lateral junction growth for the larger sliding angle is mainly caused by the further slips of asperity atoms than that with a smaller sliding angle. Overall, the simulation results provide useful insights into the atomic origins of the correlation between the evolution of the contact area and the tangential force coefficient in nanoscale contacts.

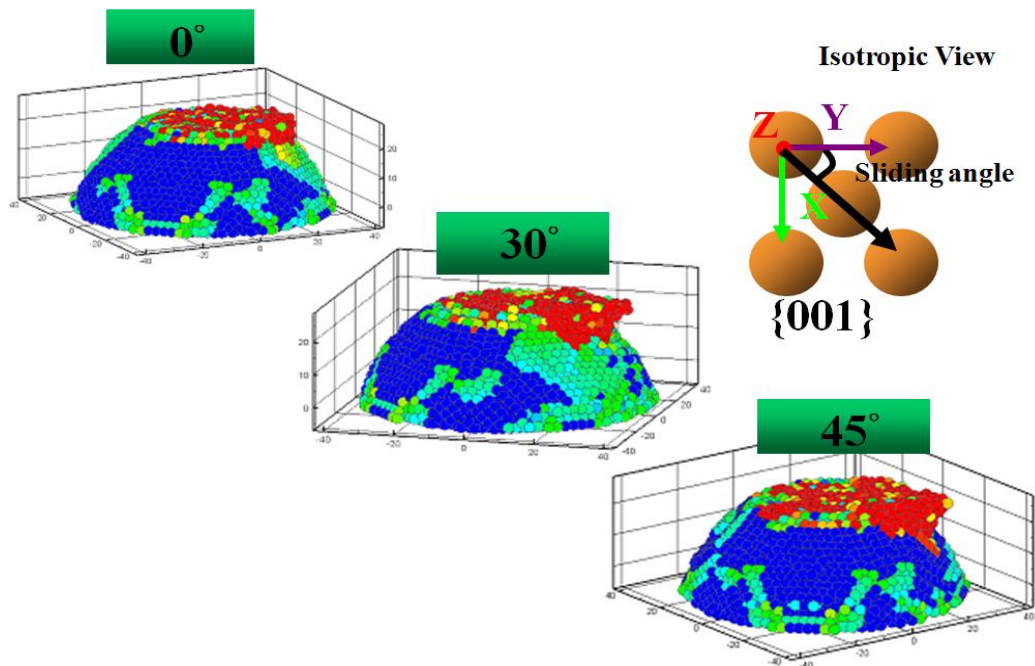


**Fig. 27: Atomistic configuration of lateral junction growth of a Cu asperity with various sliding angles.**

## References

1. I. Szlufarska, *et al.*, "Recent advances in single-asperity nanotribology," *Journal of Physics D: Applied Physics*, vol. 41, pp. 123001, 2008.
2. A. D. Romig, Jr., *et al.*, "Materials issues in microelectromechanical devices: science, engineering, manufacturability and reliability," *Acta Materialia*, vol. 51, pp. 5837-66, 2003.
3. O. Auciello, *et al.*, "Are Diamonds a MEMS' Best Friend?," *Microwave Magazine*, pp. 61-75, 2007.
4. A. V. Sumant, *et al.*, "Toward the ultimate tribological interface: Surface chemistry and nanotribology of ultrananocrystalline diamond," *Advanced Materials*, vol. 17, pp. 1039-1045, 2005.
5. O. Auciello, *et al.*, "Materials science and fabrication processes for a new MEMS technology based on ultrananocrystalline diamond thin films," *Journal of Physics Condensed Matter*, vol. 16, pp. 539-552, 2004.
6. H. D. Espinosa, *et al.*, "Mechanical properties of ultrananocrystalline diamond thin films relevant to MEMS/NEMS devices," *Experimental Mechanics*, vol. 43, pp. 256-268, 2003.
7. O. Auciello, *et al.*, "Science and technology of ultrananocrystalline diamond (UNCD) thin films for multifunctional devices," *Proceedings of the SPIE - The International Society for Optical Engineering*, vol. 4235, pp. 10-20, 2001.
8. P. J. Heaney, *et al.*, "Diamond Coatings for Micro End Mills: Enabling the Dry Machining of Aluminum at the Micro-scale," *Diamond and Related Materials*, vol. 17, pp. 223-233, 2008.
9. F. Mangolini, *et al.*, "Angle-resolved environmental X-ray photoelectron spectroscopy: A new laboratory setup for photoemission studies at pressures up to 0.4 Torr," *Review of Scientific Instruments*, vol. 83, pp. 093112, 2012.
10. J. Tersoff, "Empirical Interatomic Potential for Carbon, with Application to Amorphous Carbon," *Physical Review Letters*, vol. 61, pp. 2879-2882, 1998.
11. J. Tersoff, "New Empirical Approach for the Structure and Energy of Covalent Systems," *Physical Review B*, vol. 37, pp. 6991-7000, 1988.

12. J. Tersoff, "Modeling Solid-State Chemistry: Interatomic Potentials for Multicomponent Systems," *Physical Review B*, vol. 39, pp. 5566-5568, 1989.
13. S. Osswald, *et al.*, "Phonon confinement effects in the Raman spectrum of nanodiamond," *Physical Review B*, vol. 80, pp. 75419, 2009.
14. S. Porro, *et al.*, "Nanocrystalline diamond coating of fusion plasma facing components," *Diamond and Related Materials*, vol. 18, pp. 740-744, 2009.
15. M. E. Drew, *et al.*, "Nanocrystalline diamond AFM tips for chemical force spectroscopy: fabrication and photochemical functionalization," *Journal of Materials Chemistry*, vol. 22, pp. 12682-12688, 2012.
16. T. D. B. Jacobs, *et al.*, "The Effect of Atomic-Scale Roughness on the Adhesion of Nanoscale Asperities: A Combined Simulation and Experimental Investigation," *Tribology Letters*, vol. 50, pp. 81-93, 2013.
17. L. Pastewka, *et al.*, "Anisotropic mechanical amorphization drives wear in diamond," *Nature Materials*, vol. 10, pp. 34-38, 2011.
18. A. R. Konicek, *et al.*, "Influence of surface passivation on the friction and wear behavior of ultrananocrystalline diamond and tetrahedral amorphous carbon thin films," *Physical Review B*, vol. 85, pp. 155448, 2012.
19. A. R. Konicek, *et al.*, "Origin of ultralow friction and wear in ultrananocrystalline diamond," *Physical Review Letters*, vol. 100, pp. 235502, 2008.
20. T. Kunze, *et al.*, "Wear, Plasticity, and Rehybridization in Tetrahedral Amorphous Carbon," *Tribology Letters*, pp. 1-8, 2013.
21. W. G. Hoover, "Canonical dynamics: Equilibrium phase-space distributions," *Phys. Rev. A*, vol. 31, pp. 1695-1697, 1985.
22. C. Y. Tang, L. C. Zhang, "The Shape effects of Silicon Nanowires – A Molecular Dynamics and Density Functional Theory Study," *Nanotechnology*, vol. 16, pp. 15-20, 2005.
23. B. Luan, M. O. Robbins, "The breakdown of continuum models for mechanical contacts," *Nature*, vol. 435, pp. 929-932, 2005.
24. Y. R. Jeng, S. R. Peng, "Investigation into the lateral junction growth of single asperity contact using static atomistic simulations," *Applied Physics Letters*, vol. 94, pp. 163103, 2009.

25. B. Li, P. C. Clapp, J. A. Rifkin, X.M. Zhang, "Molecular dynamics simulation of stick-slip," *Journal of Applied Physics*, vol. 90, pp. 3090-3094, 2001.
26. D. Mulliah, S. D. Kenny, R. Smith, "Modelling of stick-slip using molecular dynamics," *Physical Review B*, vol. 69, pp. 205407, 2004.
27. R. W. Carpick, D. F. Ogletree, M. Salmeron, "Lateral stiffness: A new nanomechanical measurement with friction force microscopy," *Applied Physic Letters*, vol. 70, pp. 1548-1550, 1997.
28. A. Socoliuc, R. Bennewitz, E. Gnecco, E. Meyer, "Transition from Stick-Slip to Continuous Sliding in Atomic Friction: Entering a New Regime of Ultralow Friction," *Physical Review B*, vol. 92, pp. 134301, 2004.
29. V. Brizmer, Y. Kligerman, I. Etsion, "A model for junction growth of a spherical contact under full stick condition," *ASME Journal of Tribology*, vol. 129, pp. 783-790, 2007.
30. Y. C. Wu, G. G. Adams, "Plastic yield conditions for adhesive contacts between a rigid sphere and an elastic half-space," *ASME Journal of Tribology*, vol. 131, pp. 011403, 2009.
31. K. L. Johnson, *Contact Mechanics*, Cambridge University Press, UK, 1985.
32. Y. R. Jeng, C. M. Tan, "Investigation into the Nanoindentation Size Effect Using Static Atomistic Simulations," *Applied Physic Letters*, vol. 89, pp. 251901, 2006.